

The Novel Obscured State of Stellar-mass Black Hole GRS 1915+105

M. BALAKRISHNAN,¹ J. M. MILLER,¹ M.T. REYNOLDS,¹ E. KAMMOUN,¹ A. ZOGHBI,¹ AND B.E. TETARENKO¹

¹*Department of Astronomy, The University of Michigan, 1085 S. University Ave., Ann Arbor, MI, 48109, USA*

ABSTRACT

GRS 1915+105 is a stellar-mass black hole that is well known for exhibiting at least 12 distinct classes of X-ray variability and correlated multi-wavelength behavior. Despite such extraordinary variability, GRS 1915+105 remained one of the brightest sources in the X-ray sky. However, in early 2019, the source became much fainter, apparently entering a new accretion state. Here, we report the results of an extensive, year-long monitoring campaign of GRS 1915+105 with the *Neil Gehrels Swift Observatory*. During this interval, the flux of GRS 1915+105 gradually diminished; the observed count rate eventually dropped by two orders of magnitude. Simple but robust spectral fits to these monitoring observations show that this new state results from the combination of a dramatic and persistent increase in internal obscuration, and a reduced mass accretion rate. The internal obscuration is the dominant effect, with a median value of $N_H = 7 \times 10^{23} \text{ cm}^{-2}$. In a number of observations, the source appears to be Compton-thick. We suggest that this state should be identified as the “obscured state,” and discuss the implications of this new (or rarely observed) accretion mode for black holes across the mass scale.

Keywords: X-rays: stellar-mass black holes — X-rays: binaries — accretion – accretion disks — highly obscured — low flux

1. INTRODUCTION

Microquasars are stellar-mass black holes that replicate some of the behaviour of supermassive black holes on accessible time scales, allowing observers to better understand quasars and Active Galactic Nuclei (AGN) (Mirabel & Rodríguez 1999). GRS 1915+105 is a well-studied and well-known microquasar due to its interesting properties: apparently superluminal radio jets (Mirabel & Rodríguez 1994), distinctive X-ray variability classes (Belloni et al. 2000), high frequency QPOs (McClintock & Remillard 2006), and “heartbeats” (Zoghbi et al. 2016). The complex variability has been attributed to disk instabilities (e.g. Merloni & Nayakshin 2006) associated with the high accretion rate. Indeed, since its discovery in 1992, GRS 1915+105 has persistently been one of the brightest sources in the X-ray sky.

In July of 2018, GRS 1915+105 unexpectedly started dimming: Negoro et al. 2018 observed the lowest soft X-ray flux of GRS 1915+105 in the 22 years of monitoring with RXTE/ASM and MAXI/GSC, reporting a 2-10

keV flux of $2.4 \times 10^{-9} \text{ erg cm}^{-2} \text{ s}^{-1}$ and an unabsorbed flux of $4.3 \times 10^{-9} \text{ erg cm}^{-2} \text{ s}^{-1}$. The broad similarities between this flux decline and the decay of other transient X-ray binary outbursts led Negoro et al. 2018 to conclude that the long outburst of GRS 1915+105 was ending. However, weekly observations with NICER then showed that GRS 1915+105 appeared to stabilise to a flux of 0.08 Crab. In April 2019, there was a sudden evolution in the source: the flux dropped to $1.2 \times 10^{-9} \text{ erg cm}^{-2} \text{ s}^{-1}$ (0.5-10.0 keV), and QPOs that had previously been detected either halted or were no longer detectable (Homan et al. 2019). Contemporaneous Chandra observations found that the spectrum of GRS 1915+105 was marked by a number of strong, ionized absorption lines, potentially consistent with a slow, dense disk wind (Miller et al. 2019b, 2020).

In order to better understand this behavior, we launched a year-long X-ray monitoring campaign with the *Neil Gehrels Swift Observatory* (Gehrels et al. 2004) (hereafter *Swift*). The cadence and sensitivity afforded by *Swift* are ideal for tracing the outbursts of X-ray transients (see, e.g. Reynolds & Miller 2013); particularly when an outburst decays to low flux levels, *Swift* is the only means of obtaining monitoring that enables basic spectral modeling. Through this program, we have

previously reported evidence that GRS 1915+105 is sometimes Compton-thick in its obscured state (Miller et al. 2019a, 2020), and that the column density remains persistently high (Balakrishnan et al. 2019).

During our *Swift* monitoring campaign, a number of strong X-ray and radio flares were detected from GRS 1915+105 (see, e.g., Motta et al. 2019; Trushkin et al. 2019a,b; Takagi et al. 2020). These flares clearly signal jet activity, and they also clearly signal that the mass accretion rate onto the black hole remained relatively high despite the low flux. This is consistent with flux from the central engine becoming heavily obscured.

In this paper, we present a comprehensive spectral analysis of 118 *Swift* spectra obtained during the dim-variable period of GRS 1915+105; spanning from April 2019 through April 2020. The heavily obscured spectra that we obtained from GRS 1915+105 are very similar to spectra observed in Seyfert-2 AGN and Compton-thick AGN, so we fit each spectrum with AGN-like models including internal obscuration, scattering, and distant reflection. We traced the evolution of the model parameters across the novel obscured state, and examined correlations between the key model parameters. We also examined the light curve of each observation in order to identify flaring episodes. Section 2 details the steps taken to reduce the data and the instrumental set-up. In Section 3, we describe our analysis of the *Swift* spectra. Section 4 details the results obtained in our modelling, including the evolution of model parameters and potential correlations. In Section 5, we discuss the implications of the novel obscured state observed in GRS 1915+105.

2. DATA REDUCTION

We analyzed a total of 122 *Swift*/XRT observations of GRS 1915+105, obtained between April 2019 and April 2020, and available in the public NASA/HEASARC archive. The identification number, start time, duration, and number of photon counts of each observation are given in Table 1. For consistency and accuracy, our analysis was restricted to *Swift* observations that were obtained in WT (Windowed Timing) mode. Observations obtained in Photon Counting mode appear to occasionally suffer from photon pile-up; since it is difficult to recover the intrinsic continuum in heavily obscured spectra, pile-up mitigation is unlikely to be fully robust.

We processed all of the observations using the tools available in HEASOFT version 6.26. Initial event cleaning was carried out using the task XRTPIPELINE. We created source and background regions that measured around 60 arcseconds. Spectra and light curves were extracted using XSELECT. Ancillary response files (ARF)

were created using XRTMKARF, and finally, the spectra were binned to a signal-to-noise ratio of 3.0 using FTGROUPPHA. In each spectral fit, we used the default redistribution matrix file (RMF) for WT mode available in the *Swift* calibration data base (CALDB version 20180710).

Swift observed GRS 1915+105 122 times with WT mode during the monitoring period. After binning, 15 observations did not have enough counts for spectral analysis at a signal-to-noise ratio of $S/N \geq 3$, leaving 107 useful observations. Some of the remaining observations required additional considerations. For the small number of observations consisting of multiple good time intervals (GTIs), where possible, we analyzed each GTI separately. This was important because the internal obscuration sometimes decreased or increased significantly within the course of a single day. In the cases where one or more segments had too few counts to allow for meaningful spectroscopy, the time-averaged spectrum was analyzed. We also observed two full X-ray flares, and two segments of X-ray flares. OBSIDs 00012178006 and 00012178037 captured full flares. OBSIDs 00034292162 and 00012178019 captured the rise of a flare during the exposure. For these observations, the flare and steady emission were analyzed separately. During fitting, we noticed that four observations had the same number of degrees of freedom, and very low C/ν values, where C refers to the Cash statistic, explained in the following section. The fits also returned a null hypothesis value of 1, and the spectra have therefore been omitted.

This leaves us with 96 untouched WT-mode observations, seven observations that were split into two segments, and four observations that were separated into flare/non-flare spectra. Therefore, we present results from a total of 118 spectra.

3. ANALYSIS

All spectral fits were made using XSPEC version 12.10.1 (Arnaud 1996). In WT mode, fits are sometimes extended down to 0.6 keV (e.g., Rykoff et al. 2007; Reynolds & Miller 2013). In the case of GRS 1915+105, there are very few counts below 1 keV, so we adopted this energy as our lower fitting bound. We adopted an upper fitting bound of 10 keV, the upper limit of the calibrated XRT band. The fits minimized the Cash statistic, or “C” statistic (Cash 1979). It must be noted that in reality XSPEC uses a slightly modified version of the Cash statistic when background spectra with Poisson noise is added called the W statistic. Please see Arnaud 1996 for further details. The errors reported in this work are 1σ errors. The errors on derived quantities were calcu-

lated using standard error propagation, and are also 1 σ confidence errors.

Despite a relatively modest number of counts, it is clear that the spectra differ considerably from those typically obtained in low-mass X-ray binaries. These differences are illustrated in Figure 1, using the spectrum from OBSID 00034292201. Stellar-mass black holes in the “low/hard” state exhibit power-law continua (see Miller et al. 2013 for modeling of GRS 1915+105 in a typical “low/hard” state and Tetarenko et al. 2016 for behaviour of stellar mass black holes in this state). Fits to OBSID 00034292201 with a plausible Galactic absorbing column ($N_H = 4.35 \times 10^{22} \text{ cm}^{-2}$ and reasonable power-law index ($\Gamma = 2$) completely fail to fit the spectrum. Additional obscuration at low energy must be the result of an additional internal column of cold or low-ionization gas. The continuum in the Fe K band is altered by very strong reflection, as indicated by an Fe K emission line at 6.4 keV and edge at 7.1 keV.

As noted by Miller et al. 2020, this kind of spectrum is very similar to those obtained from heavily obscured black holes in Seyfert-2 or even Compton-thick AGN. We therefore adopted a simplified version of a set of models recently employed by Kammoun et al. 2020 to study a sample of Seyfert-2 AGN. The model consists of an additional internal column density component acting on the direct continuum, a scattered continuum component that can have a different column density, and unobscured cold reflection (via “pexmon,” see Nandra et al. 2007). In XSPEC parlance, this model can be written as follows: `phabslos × (phabs1 × cutoffpl + const × phabs2 × cutoffpl + pexmon)`.

The `phabslos` component describes line-of-sight absorption in the Milky Way, and its column is fixed at $N_H = 4.35 \times 10^{22} \text{ cm}^{-2}$ (Blum et al. 2009). The `phabs1` component describes the internal obscuration and it acts directly on the cut-off power-law continuum. In all fits made in this work, the cut-off energy was fixed at $E_{cut} = 30 \text{ keV}$ (e.g., Miller et al. 2013). In initial tests, we found that the power-law index was poorly constrained but always consistent with $\Gamma = 2.0$; this value was therefore frozen in all of our fits. The `phabs2` component group allows for scattered emission that may suffer different obscuration; the `const` factor is allowed to vary between zero and unity. The `pexmon` component is fit as a “reflection only” component, with its continuum parameters (the photon power-law index, cut-off energy, and flux normalization) linked to the values in the `cutoffpl` component). The reflection fraction was bounded to $-5 \leq R \leq 0$. The negative sign only indicates that “pexmon” was fit as a pure reflection spectrum, without its own continuum. A value of

$R = -1.0$ corresponds to the reflector covering the full 2π steradians of the sky, as seen from the emitter. The reflection inclination was fixed to $\theta = 72^\circ$ (as per Miller et al. 2013; note, however, that the spectrum is insensitive to this parameter), and the abundances were frozen at solar values. The reflection fraction was allowed to vary.

We decided this model was superior to others after in-depth investigation. Model superiority was determined using the Akaike Information Criterion (AIC) in a form seen in Emmanoulopoulos et al. 2016, where it is corrected for the bias arising from the finite size of the sample.

$$\text{AIC}_C = 2k - 2C_L + C + \frac{2k(k+1)}{N - k - 1},$$

where C_L is the constant likelihood of the true hypothetical model, and does not depend on either the data or tested models, C is the Cash statistic value, k is the number of free model parameters, and N is the number of data points. When taking the difference of the AIC of two models, the constant likelihood factor cancels out. If $\Delta\text{AIC}_C < 2$, then the models fit the data equally well. Below, we describe alternative models that were investigated, along with approximate values of the associated ΔAIC_C .

- Ionized obscuration ($\Delta\text{AIC}_C > 15$): In one trial, we changed the `phabs1` component to a `zxcipcf` component, which uses a grid of XSTAR photoionised absorption models for the absorption and assumes the gas only covers some fraction of the source. This allowed us to examine the possibility that the internal obscuration is ionized, and that it may only partially cover the central engine. In our tests, `zxcipcf` did not improve the fit; in many cases, poorer fits resulted, with $\Delta\text{AIC}_C > 15$.
- Diffuse, ionized emission ($\Delta\text{AIC}_C > 15$): We also tried adding an `apex` component (Foster et al. 2012). This would capture emission from diffuse, ionized gas, likely dominated by Fe XXV and Fe XXVI lines (see, e.g., Miller et al. 2020). The addition of this component also tended to *increase* the C-statistic. At least at the resolution and sensitivity afforded by the XRT monitoring spectra, diffuse emission is not strongly required.
- Constraining the scattering component ($\Delta\text{AIC}_C > 15$): It is reasonable to expect that the contribution of the scattered emission may be fairly minor. However, fits to the spectra with the value of the constant constrained to be less than 0.1 were significantly worse. Despite their modest sensitivity, the data prefer a de-

gree of scattered emission, and values of the constant factor that are a few times higher than this limit.

- More limited reflection fraction ($2 < \Delta\text{AIC}_C < 8$): At the beginning of our analysis, it seemed appropriate to assume that the obscuring gas formed a disk around the central engine, given that disk winds in stellar-mass black holes are generally equatorial (Miller et al. 2006; Ponti et al. 2012). We therefore bounded the reflection fraction to stay between $-1 \leq R \leq 0$. This resulted in 40% of the observations hitting the limit of $R = -1$. Given the extremity of this novel state of GRS 1915+105, a new lower limit of $-5 \leq R \leq 0$ was adopted. Improved fits were then achieved, potentially indicating that the disk wind reached large scale heights throughout the course of our observation campaign.

Figure 1 shows the spectrum obtained in OBSID 00034292201, fit with our model. An excellent fit is obtained ($C/\nu = 64.6/64$). The additional absorbing column at low energy, the Fe K emission line, and the Fe K edge are all modeled well. Moreover, the internal obscuration and reflection parameters can be constrained, and correlated.

Figure 2 helps to illustrate the features and action of this model. We searched for archival XRT spectra obtained in the “low/hard” state, with an unabsorbed flux comparable to spectra in the obscured state. OBSID 00030333242, obtained on March 23, 2016, is shown in Figure 2. Its spectrum can be fit with a simple power-law continuum, modified by absorption in the ISM. The spectrum of OBSID 00034292186, obtained on June 24, 2019, can be fit with the same power-law index *and* normalization. However, the more recent spectrum requires a very large internal column density and distant reflection, as per the models outlined above. Clearly, the internal obscuration is not only strong, but the defining characteristic of this source state, making it easy to measure even in our snapshot spectra.

In addition to measuring key parameters, we also obtain absorbed and unabsorbed flux values of the central engine. Since modeling highly obscured spectra can be particularly difficult, we only report fluxes from the 1–10 keV band used for spectral fitting. We report the unabsorbed flux of the central engine ($F_{cent,unabs}$) as the flux from the main `cutoffpl` component only, after removing both internal and line-of-sight obscuration. The flux from the scattered and reflected components is tracked separately.

Table 2 lists the continuum parameters measured from fits to the 118 *Swift*/XRT spectra of GRS 1915+105 in its obscured state. Figure 3 depicts the evolution of the key model parameters, as well as the observed and unabsorbed flux of the central engine, the ratio of those fluxes, and the Eddington fraction of the source. The Eddington fraction was calculated using the 1-10 keV unabsorbed flux of the central engine ($F_{cent,unabs}$), where we assumed a distance of $8.2^{+2}_{-1.6}$ kpc (Reid et al. 2014). The flares are shown in each plot with orange markers.

The top panel in Figure 3 shows the time evolution of the most important quantity measured in our fits, the internal column density that acts on the direct continuum (phabs_1). In this panel, it is clear that phabs_1 is initially low, only twice as high as the value in the ISM. Over a period of 40 days, the column density increases until it is consistent with being Compton-thick on MJD 58619 (a red horizontal line marks the column density at which the obscuration becomes Compton-thick, $N_{H,1} = 1.5 \times 10^{24} \text{ cm}^{-2}$). Thereafter, the internal column density is not less than $N_{H,1} \simeq 2.3 \times 10^{23} \text{ cm}^{-2}$, and it is typically much higher over the remaining span of approximately 300 days. In total, 10% of the observed spectra are consistent with being Compton-thick. These episodes are distributed fairly randomly across the monitoring period.

The column density associated with scattered emission, $N_{H,2}$, also varies. However, it is always lower than the primary obscuring column $N_{H,1}$. The reflection fraction is weakly constrained by the data. Although most values stay between $-1 < R < 0$, there are several instances of high reflection fractions, potentially signaling that the obscuring geometry has a significant vertical extent. In other observations, the reflection fraction is formally consistent with zero. This nominally indicates that the reflector is potentially highly variable.

The observed and unabsorbed flux of the central engine, their ratio, and the inferred Eddington fraction are also shown in Figure 3. The measured values are also listed in Table 3, which also lists the flux from each component of the spectral model. These parameters vary by orders of magnitude across the monitoring period, with no clear pattern. The most important and robust result is simply that obscuration reduces the observed flux by 1–2 orders of magnitude. It is the most important factor in making GRS 1915+105 faint through 2019 and 2020; a reduced mass accretion rate is only a secondary factor (also see Figure 2). Indeed, in some observations – *not* the flares, remarkably – GRS 1915+105 is nominally super-Eddington.

4. RESULTS

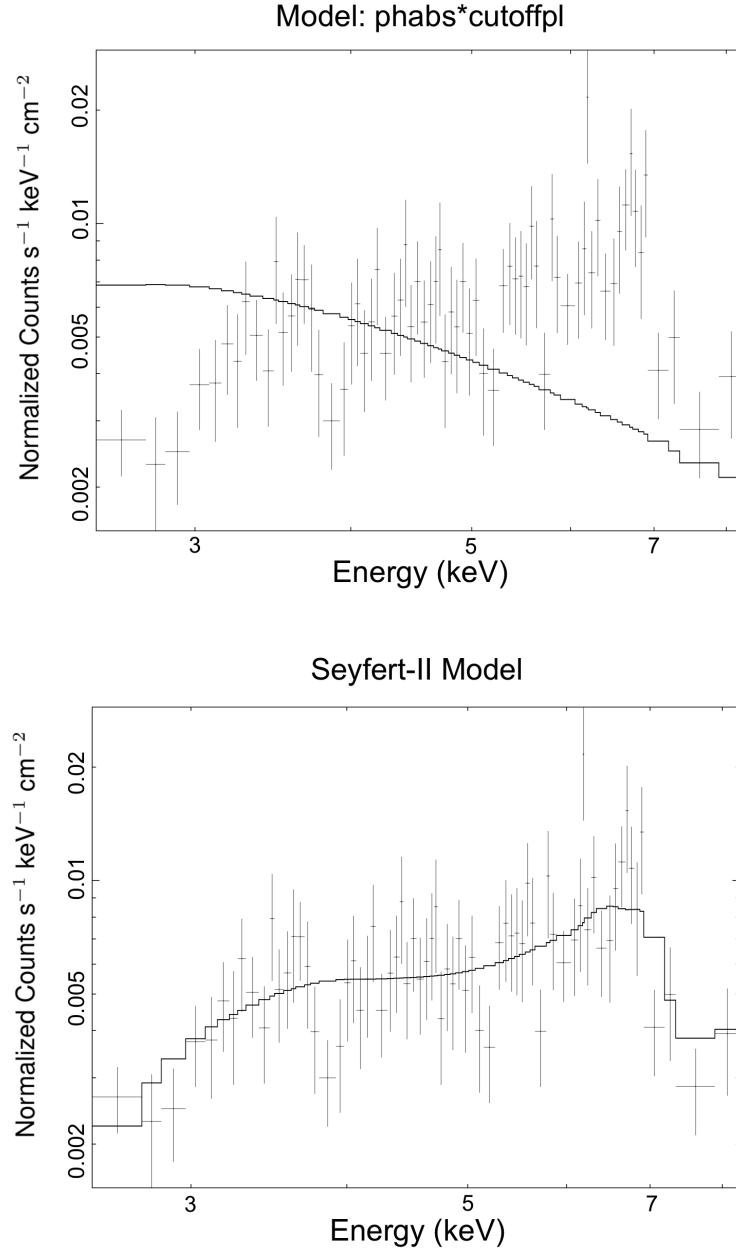


Figure 1. A *Swift*/XRT spectrum of GRS 1915+105 in the obscured state (OBS 00034292201). LEFT: The spectrum is fit with a simple model: $\text{phabs} \times \text{cutoffpl}$. The Galactic line-of-sight absorption is frozen to $N_H = 4.35 \times 10^{22} \text{cm}^{-2}$ and the cutoff energy was frozen to $E_{\text{cut}} = 30 \text{keV}$. The photon index was allowed to vary within a plausible range ($1.4 < \Gamma < 2.2$). The model fails at low energy owing to increased obscuration, and in the Fe K band owing to reflection (indicated by an Fe K emission line at 6.4 keV and Fe K edge at 7.1 keV). This model results in an unacceptable fit ($C / \nu = 323.17/68$). RIGHT: The spectrum fit with a model including internal obscuration, scattering, and reflection: $\text{phabs}_{\text{low}} \times (\text{phabs}_1 \times \text{cutoffpl} + \text{const} \times \text{phabs}_2 \times \text{cutoffpl} + \text{pexmon})$. This model achieves an excellent fit ($C / \nu = 64.63/64$).

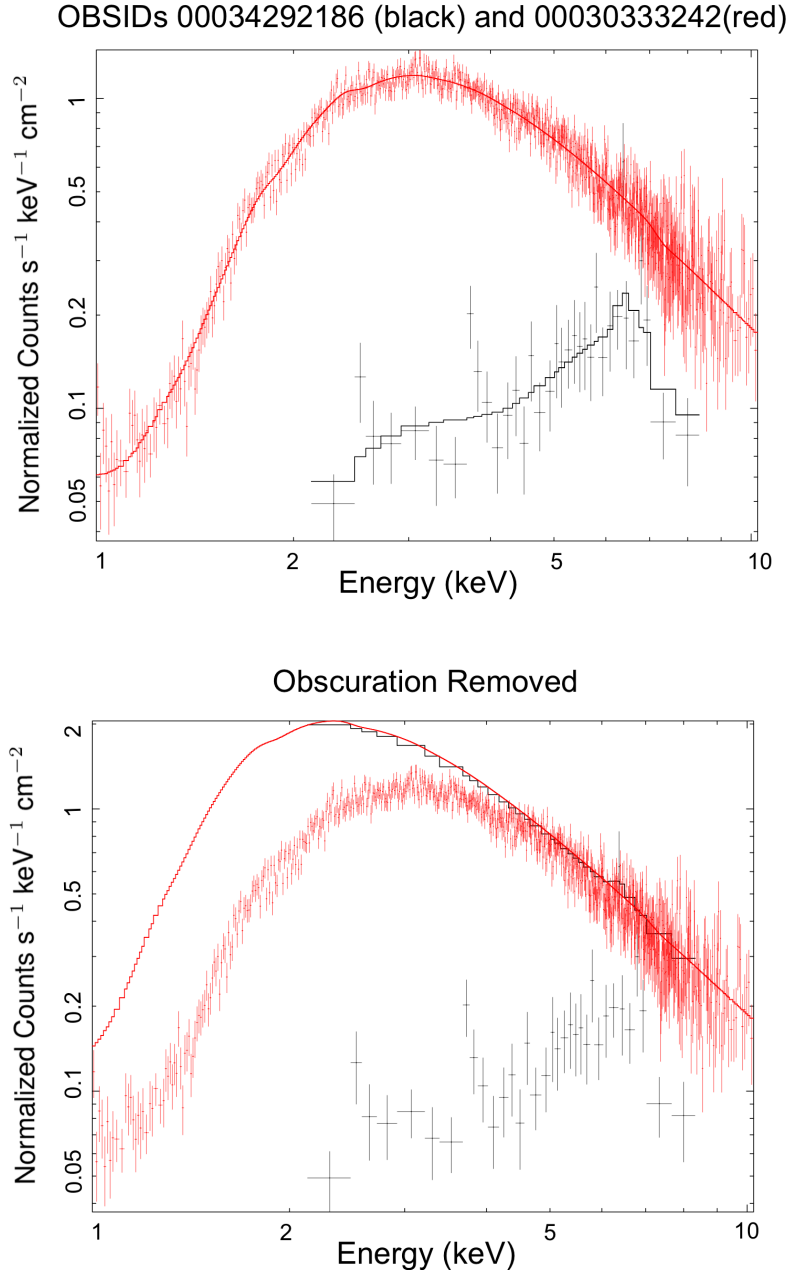


Figure 2. Two spectra of GRS 1915+105 with comparable Eddington fractions, taken twenty-six months apart. OBS 00034292186 (obtained during the obscured state, on 24 June 2019) is shown in black and 00030333242 (obtained during a normal “low/hard” state, on 23 March 2016) is shown in red. The obscured spectrum has an unabsorbed flux of 1.4×10^{-7} erg/cm²/s while the normal spectrum has an unabsorbed flux of 2.6×10^{-7} erg/cm²/s. The normal spectrum was binned to a signal-to-noise ratio of 3.0, like the other observations. The similar flux levels and spectral shapes yield very different observed spectra owing to very high internal obscuration in GRS 1915+105 throughout 2019.

4.1. Correlations

In Figure 4, we examine correlations between $N_{H,1}$, $N_{H,2}$, the reflection fraction, and the unabsorbed central engine flux. Logarithmic quantities were considered as the values of some parameters spanned orders of mag-

nitude. Observations for which $N_{H,2} \leq 10^{22}$ cm⁻² were omitted as this column density is the lower limit of what can be detected in addition to the interstellar column density. The XRT sensitivity limit is 2×10^{-14} erg cm⁻² s⁻¹ (Burrows et al. 2004), and therefore observations with reflected flux levels below this limit were omitted.

In order to concentrate on the fundamental properties of the obscuration and accretion flow, we also omitted the spectra containing flares.

Spearman Rank-Order correlation coefficients (r_s) between the parameters and corresponding p-values, the probability there is no underlying correlation, were calculated using Monte-Carlo sampling over the uncertainty of the data to account for errors. Correlation coefficients close to +1 or -1 indicate high correlation, while a coefficient of 0 indicates there is no correlation. With a significance level of $p < 0.05$, three main trends arise, presented in Figure 4. Correlations between parameters that were not significant have been omitted in the interest of space and clarity. We do note that the individual flux components are positively correlated; this is expected since the scattered and reflected components are still driven by the central engine, and these correlations are also omitted because they are easily anticipated and explained. It is clear that the reflection fraction, internal obscuration, scattered gas, and unabsorbed central engine flux are related. The internal obscuration is positively correlated with the unabsorbed central engine flux ($r_s = 0.25$) and the scattered gas ($r_s = 0.58$), while being negatively correlated with the reflection fraction ($r_s = -0.30$). This suggests that the gas that is out of the line of sight is connected to the gas in our line of sight (possibly pointing to an axially symmetric disk wind) and that stronger flux from the central engine causes an increase in gas that builds up equatorially. The correlation between internal obscuration and unabsorbed central engine flux is weak but significant, which may suggest that the flux is sometimes coupled with the absorber, but not permanently.

4.2. Flares

As noted previously, four observations captured flares. In two of these observations, the rise *and* fall of the flare was captured. Closer inspection of OBSIDs 00012178006 (MJD 58807) and 00012178037 (MJD 58935) revealed a more complex flaring structure; these observations are shown in Figure 5. The high signal to noise ratio in these light curves allowed us to calculate a decay time for the three flares seen in OBSID 00012178006 and the four flares seen in OBSID 00012178037. Using `scipy.odr` (Boggs & Rogers 1990) in python, we fit the decay of each flare with an exponential function to get a characteristic time scale. Five of the flares have decays consistent with $\tau = 20$ s, but shorter flares are also observed, leading to the conclusion that there is not a single characteristic time scale that might help to identify a flaring mechanism.

Nevertheless, it is useful to compare the flaring time scales to plausible dynamical ($t_{dyn} = \sqrt{\frac{r^3}{GM}}$), thermal ($t_{thermal} = \frac{t_{dyn}}{\alpha}$), and viscous ($t_{visc} = t_{thermal} \left(\frac{r}{h_d}\right)^2$) time scales in the disk. For an assumed viscosity parameter $\alpha = 0.1$, characteristic scale height $\frac{h_d}{r} = 0.1$, and mass of $12.4M_\odot$ (Reid et al. 2014), the viscous time scale at a radius of $r = 100 GM/c^2$ is $t_{visc} = 27$ s, comparable to the longest flares observed in our monitoring program. The dynamical and thermal time scales are much shorter, of course. This may nominally suggest that viscous fluctuations at intermediate radii play a role in the observed flaring. However, it is not clear how most of the X-ray flux could be generated at $r = 100GM/c^2$, rather than deeper within the potential. Especially given that radio flaring was observed contemporaneously with X-ray flaring (Motta et al. 2019; Trushkin et al. 2019a,b; Takagi et al. 2020), it is more likely that flares are generated in a compact corona, which may itself be the base of the jet. This does not preclude disk time scales partially determining the flaring time scales.

In Figure 6, column densities, reflection fraction, fluxes, flux ratio, and Eddington fraction are plotted for the flares. Each flare was segmented into three parts, from low to high flux. The orange, purple, and red points refer to high, medium, and low flux sections of the flares, respectively. We find that the spectral parameters of the flares do not show any clear trends. For example, a higher central engine flux does not necessarily result in lower obscuration values, or vice versa. These parameters are also listed in Table 4. Some flares may help to clear the internal obscuration (e.g., OBSID 0034292162), while others do not (e.g., OBSID 00012178006). Again, it is possible that the observed flares are not the result of a single physical process, but rather a manifestation of different processes.

In Figure 7, histograms of the primary obscuration column density, scattered column density, and reflection fraction are shown. The first eight observations are considered separately from subsequent observations that are more typical of the obscured state. Similarly, flaring segments (see below) are also considered separately. The initial observations show lower reflection fractions, potentially consistent with standard reflection from the accretion disk. Later observations extend to much larger reflection fractions, indicative of a geometry with greater vertical extent.

5. DISCUSSION

The extraordinary variability of the stellar-mass black hole GRS 1915+105 has been studied extensively, but in early 2019 it entered a new accretion state that we call

the “obscured state”, characterized by a low observed flux driven by increased internal obscuration. The spectra bear strong similarities to those typically observed in highly obscured Seyfert-2 AGN. Using a spectral model based on those sources, we find that the internal obscuration increased at the onset of the monitoring period and then remained very high, reducing the observed flux by an order of magnitude. Analysis of relevant spectral parameters revealed three main trends: (1) a positive correlation between internal obscuration and unabsorbed flux of the central engine, (2) a positive correlation between the internal obscuration and scattered gas, and (3) a negative correlation between reflection fraction and the internal obscuration. In the following section, we discuss the nature of the obscuring gas, before ending with comparisons to other astronomical objects and proposed future studies.

The obscured state appears to be driven by obscuration of the central engine, not by a drop in the mass accretion rate onto the black hole. The first few observations showed a relatively low internal obscuration column density (10^{23} cm^{-2}), but this value increased and stayed high throughout our monitoring campaign, with a median value of $7 \times 10^{23} \text{ cm}^{-2}$ (see Figure 3). The Eddington fraction, calculated using the unabsorbed direct flux from the central engine, remains relatively high during the monitoring period, with a median value of $L_{\text{Eddington}} = 0.1$. The Eddington fraction is not systematically higher early in the monitoring period, before the obscuration increases (see Figure 3).

Variations in, and correlations between, the column density and spectral components can help to reveal the nature of the obscuration and the geometry of the accretion flow. Figure 4 shows that the obscuring column density increases when the central engine is more luminous (when the unabsorbed flux from the central engine is higher). This signals that the column density and the mass accretion rate are linked, consistent with some expectations of accretion disk winds. Miller et al. 2020 recently analysed three Chandra spectra of GRS 1915+105 in the obscured state and found evidence of a failed disk wind, and suggest that this eventually envelops the central engine. The relationship observed between the obscuring column density and central engine flux is consistent with an accretion flow that is struggling to eject a disk wind, and largely failing.

Miller et al. 2020 also notes the presence of ionization lines as the source transitioned to the obscured state, and neutral and ionized emission lines once the source was clearly within the obscured state. Most of our *Swift* monitoring was obtained later, during the main part of the

obscured state. Neither the *Chandra* data nor the *Swift* data show evidence of ionized absorption in the obscured state. This supports other evidence that the accretion flow evolved significantly, potentially including changes in covering factors and column density. The ionized emission lines detected in *Chandra* and *NICER* observations in the obscured state (Miller et al. 2020; Neilsen et al. 2020) are not clearly detected in our *Swift* spectra, though they cannot be ruled out. Miller et al. 2020 attributes these lines to a failed wind, rather than disk reflection.

Variability in the obscuring column density, reflected flux, scattered flux, and correlations between these parameters may reveal aspects of the wind geometry and its evolution. Most observations had reflection fractions between -1 and 0, consistent with the expectations of an accretion disk and/or equatorial wind, but there were also several with higher reflection fractions. How can the higher reflection fractions be explained? In principle, a warped disk could create higher reflection fractions, but the data likely point to a simpler explanation: the obscuring column and scattered flux are positively correlated (see Figure 4), indicating that the geometry is axially symmetric. Variations in the scale height of a cylindrical structure could lead to reflection fractions greater than unity.

Figure 4 shows a negative correlation between the reflection fraction and the obscuring column density. This means that the reflection fraction is highest at points when the measured obscuring column is not extremal, e.g., at points when the column is not Compton-thick (we find that approximately 20% of spectra imply Compton-thick obscuration.) This may indicate that the wind settles into a more equatorial geometry when the gas is most dense, perhaps because forces that would serve to lift the gas above midplane and expel the wind are particularly overwhelmed (e.g., emergent magnetic fields might be overwhelmed by gas pressure).

In other states, the disk in GRS 1915+105 may be affected by a thermal instability (e.g., Neilsen et al. 2012; Zoghbi et al. 2016). Simulations predict that this would cause the scale height of the accretion flow to increase and decrease, as the disk empties and refills (Li et al. 2007). Although we do not observe periodic variations, the behaviour of the thermal instability could potentially contribute to or drive the variations that we have observed. Importantly, the behaviour described in Li et al. 2007 produces significant outflows dependent on the disk viscosity.

Swift is a small telescope, and it makes short exposures. We have not observed GRS 1915+105 in a bright

phase, when the count rate might compensate for a small effective area and short exposure times. Moreover, it can be difficult to uniquely decompose highly obscured spectra into different flux components, even when a fairly high level of sensitivity is achieved. It is therefore worth briefly examining if the above inferences are likely to be robust. Figure 8 plots confidence contours for N_H and reflection fraction, for observations that were taken just one day apart (ObsIDs 00034292227 and 00034292228). The contour plots were made using STEPPAR in XSPEC. We stepped through column density values from 0 to $400 \times 10^{22} \text{cm}^{-2}$ in 200 steps and reflection fraction values from -5 to 0 in 100 steps. It is clear that the values for column density exclude each other, even up to their respective 2σ errors.

The rise and fall of two flares were captured in our light curves (see Figure 5). The flares may have different emission mechanisms and absorption properties, so they were analyzed separately from the spectra that contribute to the correlations in Figure 4. The evolution of the spectral parameters of the flares is shown in Figures 6 and 7. The most important difference between the regular flux intervals and the flares is that the reflection fraction is not anti-correlated with the internal obscuration in the flaring intervals. Instead, during the flares, the column densities and reflection fractions were simultaneously low. We do not find a relationship between the internal obscuration and source luminosity; However, in a flare better observed in Neilsen et al. 2020, which analyzed one flare of GRS 1915+105 in the obscured state, a strong positive correlation between partial covering fraction and source luminosity is observed. The X-ray flares are clearly linked to strong radio flares (e.g., Motta et al. 2019), likely indicating a link to jet production. If the X-ray corona is the base of the jet, and if its scale height is greater during flaring intervals, its flux may be less subject to obscuration and the reflecting gas would subtend a smaller fraction of the solid angle. We did not detect enough flares, and did not achieve enough sensitivity within each flare, to strongly confirm or reject this hypothesis.

How does the obscured state compare to better-known states observed in stellar-mass black holes? The median value of the Eddington fraction, $L/L_{Edd} \sim 0.1$, is relatively high and either consistent with the soft (or, thermal-dominant) state or the mixed states (Remillard & McClintock 2006; Miyamoto & Kitamoto 1991; Miyamoto et al. 1993). The heavy obscuration makes it particularly difficult to detect a weak and/or cool disk component in our spectra; however, the spectra are fully consistent with a simple power-law. Very strong radio and X-ray flaring is inconsistent with the soft state, and

is rare even in mixed states. In these respects, the continuum spectrum and variability of the obscured state of GRS 1915+105 are not fully consistent with definitions of standard X-ray states.

Similar obscured states may exist in other stellar-mass black holes with low-mass companion stars. However, they may previously have been missed owing to a combination of factors. First, such states may be short in systems with short orbital periods. GRS 1915+105 happens to be the stellar-mass black hole with the longest known orbital period (for recent population studies, see Tetarenko et al. 2016; Corral-Santana et al. 2016). Second, the *Swift*/XRT is more sensitive than prior instruments that monitored X-ray binary outbursts, and its pass band extends to lower energies. It is possible that prior monitoring was largely insensitive to changing internal obscuration. Third, and most importantly, if obscured states are driven by failed winds, obscured states may be partly a matter of viewing angle. Disk winds are equatorial (see, e.g., Miller et al. 2006; Ponti et al. 2012), so obscuration would be most prominent in systems viewed at a high inclination. In systems viewed closer to the pole, strong, narrow, Fe K lines should be seen, but these may be mixed with relativistic reflection from the inner disk.

GRS 1915+105 is not the only stellar-mass black hole where in heavy internal obscuration has been observed. However, the detection of heavy obscuration in our observations of GRS 1915+105 is particularly important because it carries consequences for black holes across the mass scale. The obscuration observed in GRS 1915+105 must come from the accretion flow, not the low-mass companion star. This situation differs markedly from heavy obscuration in systems like Cygnus X-3 and V4641 Sgr (see, e.g., Morningstar et al. 2014). These sources have Wolf-Rayet and B stellar companions, respectively, and the obscuration is likely the result of the massive companion wind. It is not clear that wind-fed binaries are equally good analogies for accretion onto supermassive black holes. Therefore, future studies of this obscured state should target neutron stars or black holes that have a low mass companion, a high inclination, and a long orbital period.

V404 Cyg is another low-mass X-ray binary that harbors a black hole in a wide orbit. It has also displayed evidence of strong and potentially Compton-thick internal obscuration, but only at points when the source was significantly super-Eddington (see, e.g., King et al. 2015; Motta et al. 2017). Few X-ray binaries have shown super-Eddington phases, and the same is true of AGN (Hickox et al. 2009). It is unclear if the obscured state in GRS 1915+105 and the brief Compton-thick episodes

observed in V404 Cyg are fundamentally similar but and differ only in degree. However, the fact that obscured states are possible at very different mass accretion rates in stellar-mass black holes signals that obscuration in Seyfert-2 AGN and Compton-thick AGN may not only be a matter of viewing angle, but also a matter of evolutionary phase and the nature of the innermost accretion flow.

We thank Director Brad Cenko and the *Swift* mission planning team for executing this monitoring program, especially at a time when in-person operations and meetings became impossible. We also thank the anonymous referee for comments that improved the manuscript. JMM acknowledges helpful conversations with Tahir Yaqoob and Richard Mushotzky. Mayura Balakrishnan thanks Lia Corrales for helpful conversations.

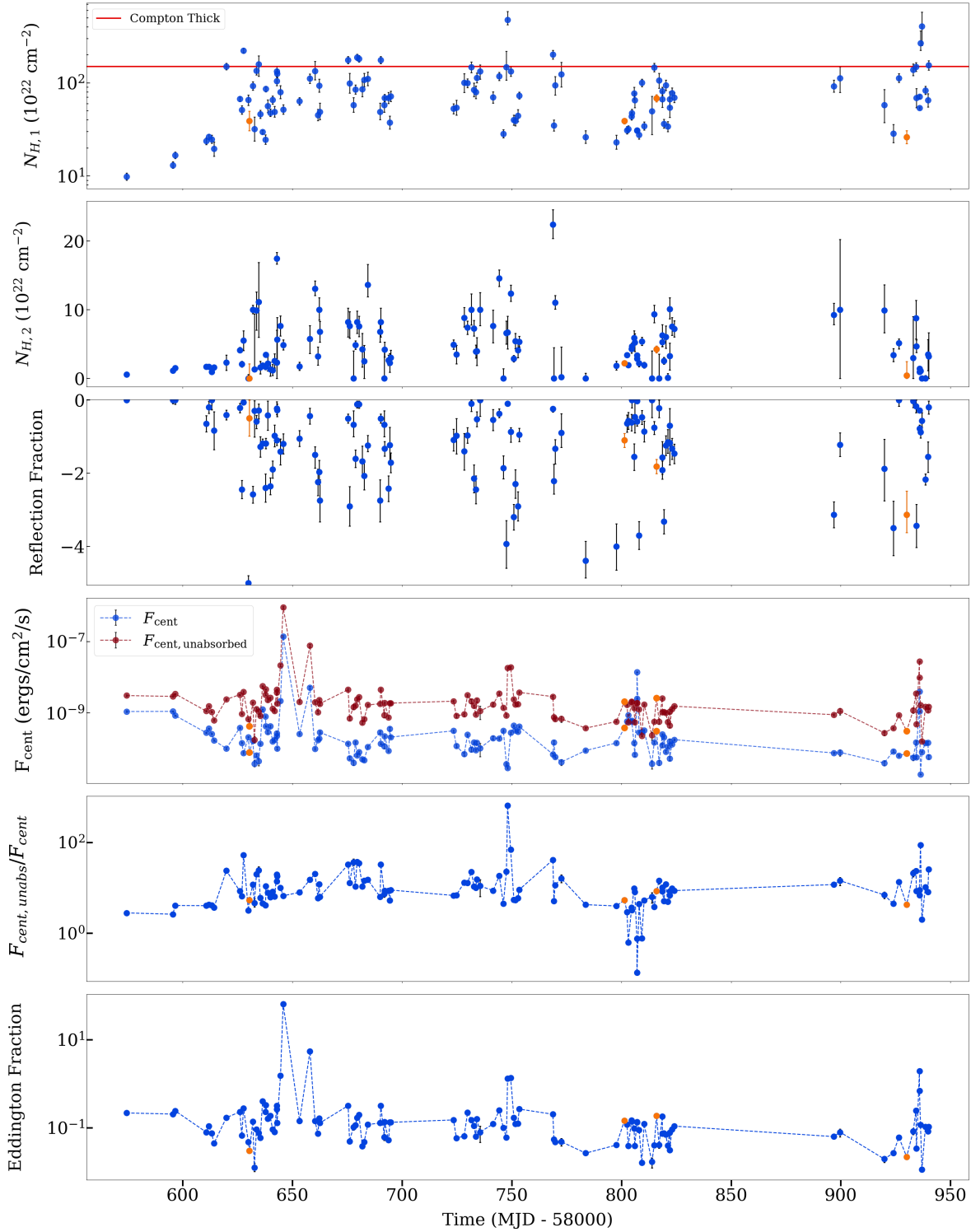


Figure 3. Continuum parameters and fluxes are plotted for all spectra. In descending order, we plot values for the two *phabs* column densities, the reflection fraction, the 1-10 keV absorbed and unabsorbed fluxes of the central engine (F_{cent} and $F_{cent,unabs}$), the unabsorbed to absorbed flux ratio ($F_{cent,unabs}/F_{cent}$), and the Eddington fraction calculated using the 1-10 keV unabsorbed flux. The points in orange correspond to spectra where a flare was observed in the light curve. The red line in the first panel denotes the measure of one Thompson optical depth.

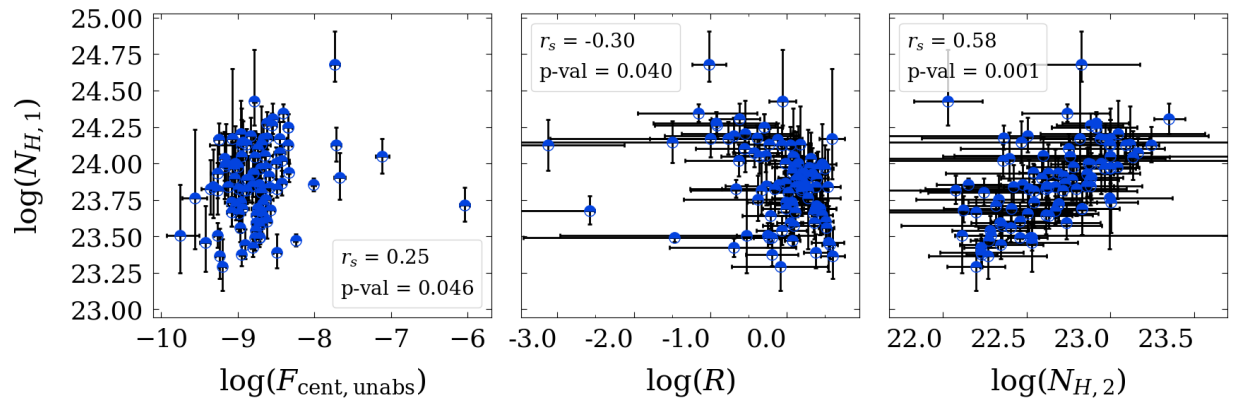


Figure 4. Correlations between internal obscuration and $F_{\text{unabsorbed,central}}$, reflection fraction, and scattered gas are shown. All values are in logspace. The Spearman Rank-Order correlation coefficient, r_s is shown for each correlation, along with the probability of false correlation.

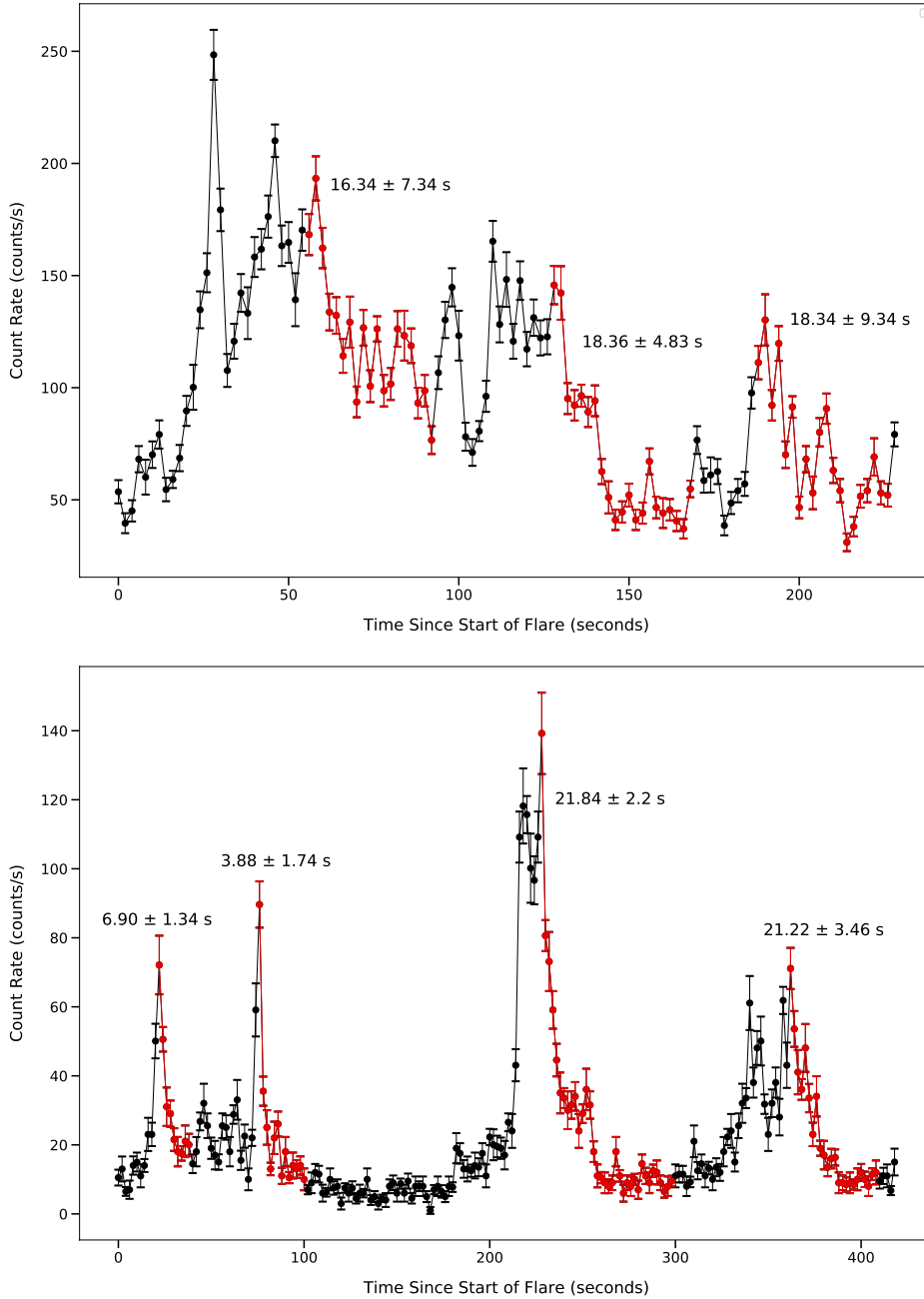


Figure 5. Light curves of the flares captured in OBSIDs 00012178006 and 00012178037. The light curves were extracted using XSELECT and XRONOS. The light curves are plotted in units of count rate, with time bins of $\Delta t = 2$ s. The high signal-to-noise ratio allowed us to analyse multiple components of the flares separately. Data shown in red indicates the portions that were fit with an exponential function, and the text nearby reports the decay time that resulted, in seconds. Note that the x-axis indicates the time since the start of the flare, not the start of the observation that these flares were captured in.

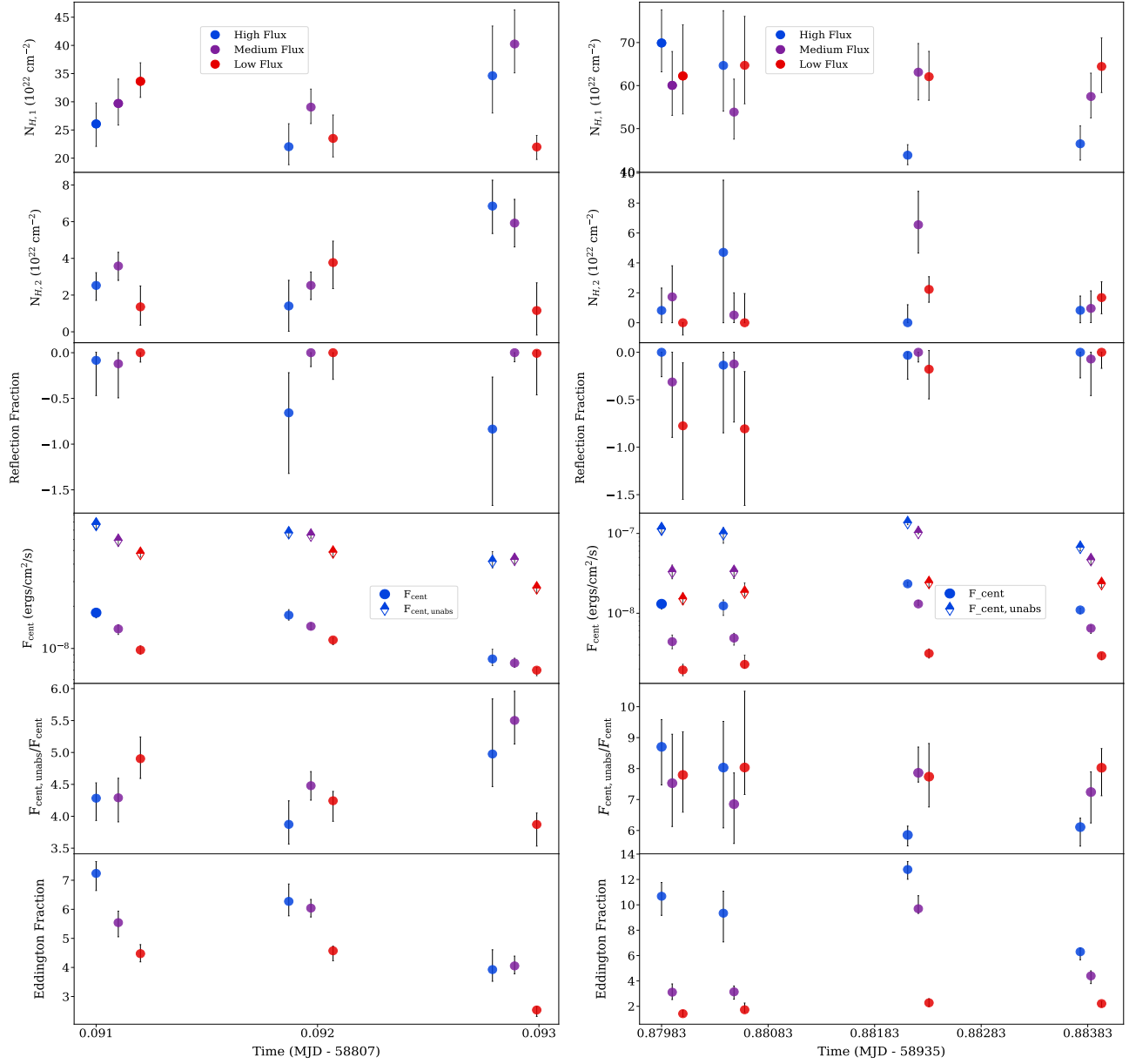


Figure 6. Spectral parameters for flares seen in OBSID 00012178006 (left) and OBSID 00012178037 (right). The orange, purple, and red points refer to high flux, medium flux, and low flux sections of the flare, respectively. In the flux panel, the circular markers and diamond markers refer to the absorbed and unabsorbed flux of the central engine, respectively. There is no clear trend to be observed. Compared to other spectra, flares seem to have on average, lower obscuration, and a more disk-like reflector.

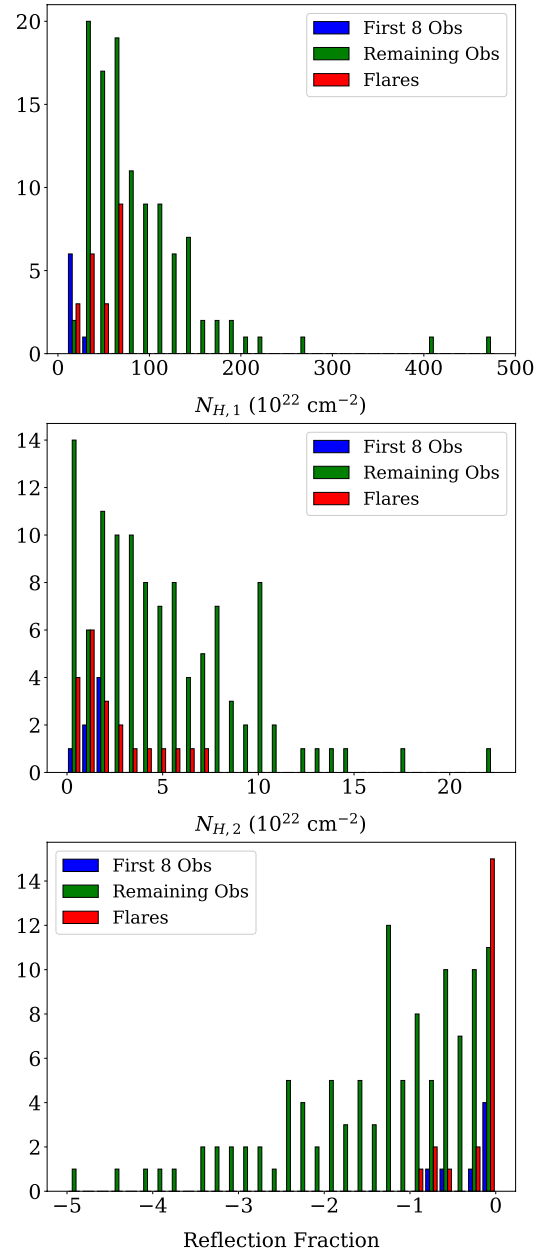


Figure 7. Histogram of column densities and reflection fraction. The y-axis refers to the number of observations. The first few observations (which roughly correspond to the first month of the monitoring campaign) have lower obscuration values and smaller reflection fractions, similar to the flares.

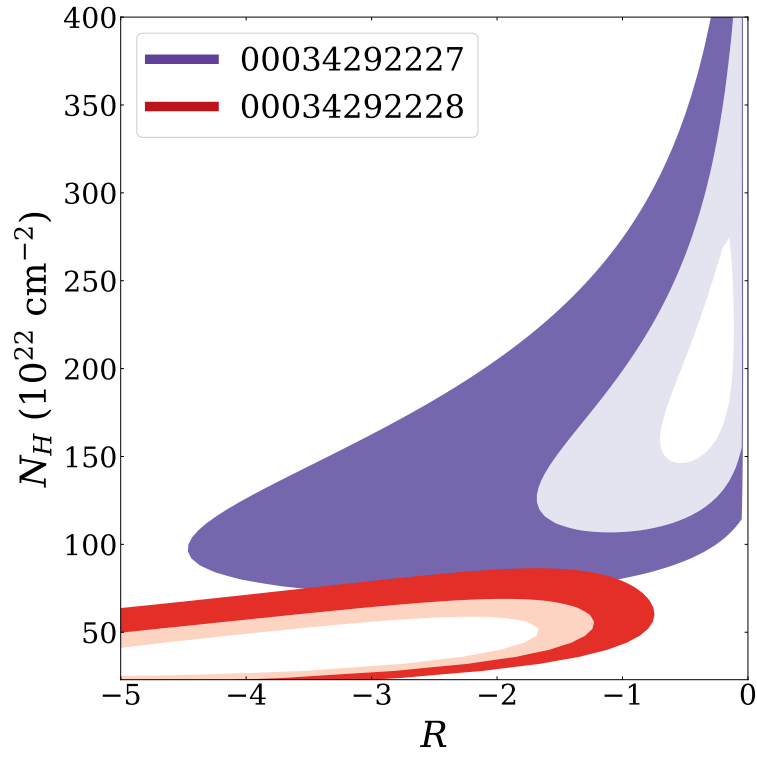


Figure 8. Contour plot showing column density vs. reflection fraction for observations 00034292227 and 00034292228, taken one day apart. The column densities are distinctly different up to 2σ error bars, justifying the high values for internal obscuration returned by some of the fits.

Table 1. List of *Swift* observations

OBSID	MJD - 58000	Exposure Time	Photon Counts
00094149013	58574	1700	27000
00088850001	58596	2100	33000
00094149014	58597	1900	23000
00034292127	58611	2000	7900
00034292129	58612	1900	7900
00034292131	58613	1000	3900
00034292133	58614	870	2400
00034292136	58620	860	720
00034292140	58626	990	3400
00034292142	58627	2000	3200
00034292143	58628	990	530
00034292146	58630	960	2500
00034292148	58630	620	430
00034292150	58632	980	2700
00034292152	58633	980	190
00034292154	58634	1100	580
00034292156	58635	870	180
00034292158	58635	980	1100
00034292160	58636	980	13000
00034292162	58638	710	4400
00034292162 (flare)	58638	240	2300
00034292164	58639	160	430
00034292166	58640	470	1800
00034292168	58641	970	1500
00034292170	58642	970	1100
00034292172a	58643	480	1600
00034292172b	58643	420	540
00034292174	58643	760	510
00034292176	58645	1000	860
00034292178	58646	200	1700
00034292184	58653	1100	1400
00034292186	58658	850	480
00034292188	58660	250	570
00034292189	58662	700	1300
00034292190a	58662	370	1000
00034292190b	58662	480	1600
00034292192	58675	720	490
00034292194	58676	880	540
00034292193	58678	1000	1900

Table 1 continued

Table 1 (*continued*)

OBSID	MJD - 58000	Exposure Time	Photon Counts
00034292195	58679	890	2000
00034292196	58679	1000	650
00034292197	58680	940	530
00034292198	58682	1000	570
00034292199	58683	900	590
00034292201	58684	970	840
00034292205a	58690	250	820
00034292205b	58690	520	730
00034292206	58692	330	220
00034292207	58692	980	1700
00034292208	58694	970	1200
00034292209a	58694	190	520
00034292209b	58695	520	1100
00034292210	58723	460	1600
00034292211	58725	440	550
00034292212	58728	420	370
00034292213	58730	450	1300
00034292214	58732	460	240
00034292215	58733	440	1000
00034292216	58734	730	950
00034292217	58734	490	410
00034292218	58735	400	200
00034292222	58742	450	560
00034292223	58744	430	700
00034292224	58746	440	1100
00034292225	58748	460	570
00034292226	58748	440	350
00034292227	58750	420	780
00034292228	58751	440	2800
00034292229	58752	440	1500
00034292230	58753	420	1400
00034292231	58753	500	1900
00034292235	58769	780	470
00034292236	58769	810	720
00034292237	58770	700	610
00034292239	58773	1600	120
00034292240	58784	940	1000
00034292242	58798	950	1600
00012178001	58801	950	3500
00012178002	58803	850	4300
00012178003	58803	700	2700

Table 1 continued

Table 1 (*continued*)

OBSID	MJD - 58000	Exposure Time	Photon Counts
00034292243a	58805	480	2100
00034292243b	58805	350	1800
00012178004	58806	490	880
00012178005	58806	730	460
00012178006	58807	670	11000
00012178006 (flare)	58807	300	25000
00012178007	58808	700	2600
00012178008	58809	810	1400
00012178009	58810	960	2000
00012178011	58814	900	220
00012178012	58815	970	760
00012178014	58816	980	3500
00012178015	58817	890	220
00034292245a	58819	560	2000
00034292245b	58819	510	700
00012178016	58819	1000	2800
00012178017	58820	1000	850
00012178018	58821	910	900
00012178019	58822	650	290
00012178019 (flare)	58822	280	390
00012178020	58823	880	1100
00012178021	58824	920	1700
00088850006	58897	1000	1100
00088850005	58900	1800	380
00012178030	58920	970	66
00012178031	58924	850	52
00012178032	58927	800	640
00012178033	58930	900	690
00012178034	58933	550	150
00012178036a	58934	330	360
00012178036b	58934	810	910
00012178037 (flare)	58936	390	9000
00012178037	58936	460	4700
00012178038	58936	900	2100
00012178039	58937	690	670
00012178040	58939	930	1500
00012178041	58940	880	680
00012178042	58940	590	250

NOTE—The table above lists the observation ID's, start time of observations (in units of MJD), exposure time, and photon counts for each observation used in our analysis. The observation campaign we used started in April 2019 and lasted for one year.

Table 2. Continuum parameters

OBSID	MJD (58000)	$N_{H,1}$ (10^{22} cm^{-2})	$N_{H,2}$ (10^{22} cm^{-2})	factor	R	C/nu
00094149013	58574	10 $^{+1}_{-1}$	0.6 $^{+0.2}_{-0.2}$	0.6 $^{+0.1}_{-0.1}$	0.0 $^{+0}_{-0.1}$	623/626 = 0.996
00088850001	58596	13 $^{+1}_{-1}$	1.1 $^{+0.2}_{-0.2}$	0.6 $^{+0.1}_{-0.1}$	0.0 $^{+0}_{-0.1}$	731/659 = 1.11
00094149014	58597	17 $^{+1}_{-1}$	1.5 $^{+0.2}_{-0.2}$	0.5 $^{+0.1}_{-0.1}$	0.0 $^{+0}_{-0.1}$	627/612 = 1.025
00034292127	58611	24 $^{+2}_{-2}$	1.7 $^{+0.2}_{-0.2}$	0.47 $^{+0.02}_{-0.02}$	-0.7 $^{+0.2}_{-0.2}$	456/417 = 1.094
00034292129	58612	26 $^{+2}_{-2}$	1.7 $^{+0.2}_{-0.2}$	0.31 $^{+0.01}_{-0.01}$	-0.2 $^{+0.2}_{-0.2}$	450/436 = 1.033
00034292131	58613	25 $^{+3}_{-2}$	0.9 $^{+0.2}_{-0.2}$	0.42 $^{+0.02}_{-0.02}$	0.0 $^{+0.0}_{-0.3}$	271/269 = 1.009
00034292133	58614	20 $^{+4}_{-3}$	1.6 $^{+0.3}_{-0.3}$	0.6 $^{+0.1}_{-0.1}$	-0.8 $^{+0.5}_{-0.5}$	144/170 = 0.851
00034292136	58620	150 $^{+10}_{-10}$	2 $^{+1}_{-1}$	0.06 $^{+0.01}_{-0.01}$	-0.4 $^{+0.1}_{-0.1}$	37/38 = 0.982
00034292140	58626	67 $^{+4}_{-4}$	4.1 $^{+0.4}_{-0.4}$	0.16 $^{+0.01}_{-0.01}$	-0.2 $^{+0.1}_{-0.1}$	251/239 = 1.053
00034292142	58627	52 $^{+5}_{-5}$	2.1 $^{+0.4}_{-0.4}$	0.16 $^{+0.02}_{-0.02}$	-2.4 $^{+0.2}_{-0.3}$	236/202 = 1.169
00034292143	58628	220 $^{+10}_{-10}$	6 $^{+1}_{-2}$	0.03 $^{+0.01}_{-0.01}$	-0.1 $^{+0.1}_{-0.1}$	33/34 = 0.973
00034292146	58630	66 $^{+8}_{-8}$	0 $^{+1}_{-0}$	0.10 $^{+0.02}_{-0.01}$	-5.0 $^{+0.2}_{-0.0}$	182/177 = 1.031
00034292148	58630	39 $^{+11}_{-9}$	0 $^{+2}_{-0}$	0.19 $^{+0.05}_{-0.02}$	-0.5 $^{+0.5}_{-0.5}$	30/25 = 1.221
00034292150	58632	93 $^{+11}_{-10}$	10 $^{+1}_{-1}$	0.20 $^{+0.02}_{-0.03}$	-2.6 $^{+0.2}_{-0.2}$	219/200 = 1.099
00034292152	58633	32 $^{+11}_{-8}$	1.3 $^{+8.1}_{-0.1}$	0.11 $^{+0.12}_{-0.04}$	-0.3 $^{+0.3}_{-0.7}$	2/6 = 0.398
00034292154	58634	140 $^{+20}_{-20}$	10 $^{+3}_{-3}$	0.07 $^{+0.01}_{-0.02}$	-0.6 $^{+0.2}_{-0.2}$	48/35 = 1.387
00034292156	58635	160 $^{+40}_{-40}$	11 $^{+6}_{-5}$	0.07 $^{+0.05}_{-0.04}$	-0.3 $^{+0.2}_{-0.2}$	10/11 = 0.929
00034292158	58635	46 $^{+5}_{-4}$	2 $^{+1}_{-1}$	0.07 $^{+0.02}_{-0.02}$	-1.3 $^{+0.3}_{-0.3}$	75/84 = 0.905
00034292160	58636	30 $^{+1}_{-1}$	1.9 $^{+0.2}_{-0.2}$	0.17 $^{+0.01}_{-0.01}$	-1.2 $^{+0.1}_{-0.1}$	724/577 = 1.256
00034292162	58638	25 $^{+3}_{-3}$	1.7 $^{+0.4}_{-0.4}$	0.24 $^{+0.03}_{-0.03}$	-2.4 $^{+0.4}_{-0.4}$	193/318 = 0.609
00034292162 (flare)	58638	86 $^{+6}_{-5}$	3.5 $^{+0.3}_{-0.3}$	0.19 $^{+0.01}_{-0.01}$	-1.2 $^{+0.1}_{-0.2}$	359/178 = 2.018
00034292164	58639	57 $^{+9}_{-8}$	2 $^{+1}_{-1}$	0.14 $^{+0.03}_{-0.03}$	-0.4 $^{+0.4}_{-0.4}$	40/32 = 1.252
00034292166	58640	48 $^{+5}_{-4}$	1 $^{+1}_{-1}$	0.04 $^{+0.01}_{-0.01}$	-2.4 $^{+0.2}_{-0.2}$	168/144 = 1.171
00034292168	58641	66 $^{+7}_{-6}$	1 $^{+1}_{-1}$	0.06 $^{+0.02}_{-0.01}$	-1.9 $^{+0.2}_{-0.2}$	146/111 = 1.321
00034292170	58642	49 $^{+7}_{-6}$	3 $^{+1}_{-1}$	0.11 $^{+0.02}_{-0.02}$	-1.0 $^{+0.3}_{-0.3}$	73/72 = 1.019
00034292172a	58643	130 $^{+20}_{-20}$	18 $^{+1}_{-1}$	0.25 $^{+0.02}_{-0.02}$	-1.1 $^{+0.1}_{-0.1}$	127/113 = 1.124
00034292172b	58643	100 $^{+10}_{-10}$	2 $^{+5}_{-5}$	0.06 $^{+0.03}_{-0.02}$	-0.2 $^{+0.2}_{-0.2}$	24/29 = 0.853
00034292174	58643	130 $^{+10}_{-10}$	6 $^{+3}_{-4}$	0.07 $^{+0.02}_{-0.02}$	-0.3 $^{+0.2}_{-0.2}$	28/39 = 0.742
00034292176	58645	80 $^{+13}_{-12}$	8 $^{+2}_{-2}$	0.18 $^{+0.04}_{-0.04}$	-1.4 $^{+0.4}_{-0.4}$	59/61 = 0.974
00034292178	58646	52 $^{+6}_{-6}$	5 $^{+1}_{-1}$	0.17 $^{+0.03}_{-0.02}$	-1.2 $^{+0.3}_{-0.3}$	144/136 = 1.063
00034292184	58653	64 $^{+6}_{-6}$	2 $^{+1}_{-1}$	0.09 $^{+0.01}_{-0.01}$	-1.1 $^{+0.2}_{-0.2}$	119/95 = 1.26
00034292186	58658	110 $^{+10}_{-10}$	6 $^{+2}_{-2}$	0.08 $^{+0.02}_{-0.02}$	-0.4 $^{+0.2}_{-0.2}$	37/30 = 1.246
00034292188	58660	140 $^{+40}_{-30}$	13 $^{+1}_{-1}$	0.35 $^{+0.04}_{-0.09}$	-1.5 $^{+0.2}_{-0.4}$	47/44 = 1.072
00034292189	58662	45 $^{+7}_{-6}$	3 $^{+1}_{-1}$	0.09 $^{+0.03}_{-0.02}$	-2.2 $^{+0.4}_{-0.4}$	113/92 = 1.238
00034292190a	58662	94 $^{+16}_{-14}$	10 $^{+2}_{-2}$	0.21 $^{+0.03}_{-0.04}$	-2.0 $^{+0.4}_{-0.4}$	82/89 = 0.931
00034292190b	58662	49 $^{+11}_{-9}$	7 $^{+2}_{-2}$	0.23 $^{+0.06}_{-0.05}$	-2.7 $^{+0.6}_{-0.6}$	63/138 = 0.46
00034292192	58675	180 $^{+20}_{-20}$	8 $^{+2}_{-2}$	0.06 $^{+0.02}_{-0.01}$	-0.5 $^{+0.1}_{-0.1}$	73/33 = 2.214
00034292194	58676	99 $^{+28}_{-21}$	7 $^{+2}_{-2}$	0.12 $^{+0.06}_{-0.06}$	-2.9 $^{+0.5}_{-0.5}$	32/33 = 0.979

Table 2 continued

Table 2 (continued)

OBSID	MJD (58000)	$N_{H,1}$ (10^{22} cm $^{-2}$)	$N_{H,2}$ (10^{22} cm $^{-2}$)	factor	R	C/nu
00034292193	58678	58 $^{+11}_{-9}$	0 $^{+4}_{-0}$	0.03 $^{+0.03}_{-0.01}$	-0.7 $^{+0.4}_{-0.3}$	22/143 = 0.155
00034292195	58679	85 $^{+10}_{-9}$	5 $^{+1}_{-1}$	0.19 $^{+0.02}_{-0.02}$	-1.6 $^{+0.2}_{-0.2}$	153/132 = 1.16
00034292196	58679	190 $^{+20}_{-10}$	8 $^{+2}_{-2}$	0.07 $^{+0.01}_{-0.01}$	-0.1 $^{+0.1}_{-0.1}$	61/46 = 1.339
00034292197	58680	180 $^{+20}_{-10}$	8 $^{+2}_{-2}$	0.05 $^{+0.01}_{-0.01}$	-0.1 $^{+0.1}_{-0.1}$	36/35 = 1.041
00034292198	58682	86 $^{+17}_{-15}$	4 $^{+2}_{-3}$	0.12 $^{+0.04}_{-0.04}$	-1.7 $^{+0.4}_{-0.4}$	48/42 = 1.149
00034292199	58683	110 $^{+20}_{-20}$	2 $^{+2}_{-3}$	0.1 $^{+0.04}_{-0.03}$	-2.1 $^{+0.4}_{-0.4}$	45/42 = 1.072
00034292201	58684	110 $^{+20}_{-20}$	14 $^{+3}_{-2}$	0.3 $^{+0.04}_{-0.03}$	-1.2 $^{+0.3}_{-0.2}$	70/65 = 1.09
00034292205a	58690	49 $^{+11}_{-9}$	7 $^{+2}_{-2}$	0.23 $^{+0.06}_{-0.05}$	-2.7 $^{+0.6}_{-0.6}$	63/56 = 1.135
00034292205b	58690	180 $^{+20}_{-20}$	8 $^{+2}_{-2}$	0.06 $^{+0.02}_{-0.01}$	-0.5 $^{+0.1}_{-0.1}$	73/50 = 1.461
00034292206	58692	58 $^{+11}_{-9}$	0 $^{+4}_{-0}$	0.03 $^{+0.03}_{-0.01}$	-0.7 $^{+0.4}_{-0.3}$	22/15 = 1.479
00034292207	58692	69 $^{+7}_{-6}$	4 $^{+1}_{-1}$	0.07 $^{+0.02}_{-0.01}$	-1.3 $^{+0.2}_{-0.2}$	138/120 = 1.158
00034292208	58694	69 $^{+10}_{-9}$	3 $^{+1}_{-1}$	0.15 $^{+0.03}_{-0.02}$	-2.4 $^{+0.4}_{-0.4}$	107/93 = 1.153
00034292209a	58694	38 $^{+6}_{-6}$	2 $^{+1}_{-1}$	0.11 $^{+0.04}_{-0.03}$	-1.2 $^{+0.5}_{-0.5}$	40/47 = 0.862
00034292209b	58695	72 $^{+10}_{-9}$	3 $^{+1}_{-1}$	0.08 $^{+0.02}_{-0.02}$	-1.7 $^{+0.3}_{-0.3}$	107/96 = 1.121
00034292210	58723	53 $^{+7}_{-6}$	5 $^{+1}_{-1}$	0.22 $^{+0.03}_{-0.03}$	-1.1 $^{+0.3}_{-0.3}$	143/122 = 1.175
00034292211	58725	54 $^{+11}_{-9}$	4 $^{+1}_{-1}$	0.20 $^{+0.05}_{-0.04}$	-1.0 $^{+0.5}_{-0.5}$	58/46 = 1.271
00034292212	58728	100 $^{+30}_{-20}$	9 $^{+2}_{-1}$	0.2 $^{+0.1}_{-0.1}$	-1.4 $^{+0.5}_{-0.5}$	28/27 = 1.037
00034292213	58730	100 $^{+10}_{-10}$	7 $^{+1}_{-1}$	0.16 $^{+0.02}_{-0.02}$	-1.0 $^{+0.2}_{-0.2}$	108/109 = 0.997
00034292214	58732	150 $^{+20}_{-20}$	10 $^{+2}_{-2}$	0.06 $^{+0.02}_{-0.03}$	-0.1 $^{+0.1}_{-0.2}$	15/16 = 0.994
00034292215	58733	85 $^{+15}_{-13}$	7 $^{+1}_{-1}$	0.23 $^{+0.04}_{-0.04}$	-2.2 $^{+0.4}_{-0.4}$	101/89 = 1.142
00034292216	58734	80 $^{+14}_{-12}$	4 $^{+1}_{-1}$	0.15 $^{+0.03}_{-0.03}$	-2.44 $^{+0.38}_{-0.38}$	86/80 = 1.08
00034292217	58734	110 $^{+10}_{-10}$	4 $^{+2}_{-2}$	0.04 $^{+0.02}_{-0.02}$	-0.5 $^{+0.2}_{-0.2}$	31/30 = 1.044
00034292218	58735	130 $^{+20}_{-20}$	10 $^{+3}_{-2}$	0.18 $^{+0.03}_{-0.04}$	0.0 $^{+0.0}_{-0.4}$	9/12 = 0.816
00034292222	58742	70 $^{+10}_{-9}$	8 $^{+2}_{-2}$	0.08 $^{+0.03}_{-0.03}$	-0.5 $^{+0.3}_{-0.3}$	53/47 = 1.148
00034292223	58744	120 $^{+10}_{-10}$	15 $^{+1}_{-1}$	0.13 $^{+0.02}_{-0.01}$	-0.4 $^{+0.1}_{-0.1}$	48/54 = 0.892
00034292224	58746	28 $^{+3}_{-3}$	0 $^{+1}_{-0}$	0.05 $^{+0.02}_{-0.01}$	-1.9 $^{+0.3}_{-0.3}$	92/94 = 0.982
00034292225	58748	150 $^{+70}_{-40}$	7 $^{+2}_{-2}$	0.2 $^{+0.1}_{-0.1}$	-3.9 $^{+0.6}_{-0.7}$	39/43 = 0.915
00034292226	58748	480 $^{+100}_{-60}$	7 $^{+3}_{-4}$	0.01 $^{+0.0}_{-0.0}$	-0.11 $^{+0.02}_{-0.02}$	41/26 = 1.601
00034292227	58750	130 $^{+20}_{-20}$	12 $^{+1}_{-1}$	0.14 $^{+0.02}_{-0.04}$	-0.9 $^{+0.1}_{-0.3}$	63/65 = 0.979
00034292228	58751	40 $^{+5}_{-5}$	3 $^{+1}_{-1}$	0.25 $^{+0.03}_{-0.03}$	-3.2 $^{+0.4}_{-0.4}$	289/223 = 1.296
00034292229	58752	39 $^{+5}_{-4}$	5 $^{+1}_{-1}$	0.17 $^{+0.04}_{-0.03}$	-2.3 $^{+0.4}_{-0.4}$	157/128 = 1.228
00034292230	58753	45 $^{+7}_{-6}$	4 $^{+1}_{-1}$	0.14 $^{+0.03}_{-0.03}$	-2.9 $^{+0.4}_{-0.4}$	134/121 = 1.112
00034292231	58753	73 $^{+6}_{-6}$	5 $^{+1}_{-1}$	0.11 $^{+0.02}_{-0.02}$	-1.0 $^{+0.2}_{-0.2}$	171/158 = 1.085
00034292235	58769	20 $^{+20}_{-20}$	22 $^{+2}_{-2}$	0.09 $^{+0.02}_{-0.02}$	-0.2 $^{+0.1}_{-0.1}$	40/38 = 1.067
00034292236	58769	35 $^{+5}_{-4}$	0 $^{+5}_{-0}$	0.05 $^{+0.04}_{-0.01}$	-2.2 $^{+0.5}_{-0.4}$	54/59 = 0.929
00034292237	58770	94 $^{+23}_{-20}$	11 $^{+1}_{-1}$	0.32 $^{+0.05}_{-0.06}$	-1.3 $^{+0.3}_{-0.4}$	51/49 = 1.047
00034292239	58773	120 $^{+40}_{-30}$	0.2 $^{+4.4}_{-0.1}$	0.06 $^{+0.08}_{-0.02}$	-0.9 $^{+0.5}_{-0.4}$	3/6 = 0.513
00034292240	58784	26 $^{+5}_{-4}$	0.0 $^{+1}_{-0.0}$	0.11 $^{+0.03}_{-0.01}$	-4.4 $^{+0.5}_{-0.5}$	92/79 = 1.172
00034292242	58798	23 $^{+4}_{-4}$	2 $^{+1}_{-1}$	0.33 $^{+0.05}_{-0.05}$	-4.0 $^{+0.6}_{-0.6}$	123/120 = 1.03
00012178001	58801	39 $^{+3}_{-3}$	2.2 $^{+0.4}_{-0.4}$	0.14 $^{+0.01}_{-0.01}$	-1.1 $^{+0.19}_{-0.19}$	305/262 = 1.164

Table 2 continued

Table 2 (continued)

OBSID	MJD (58000)	$N_{H,1}$ (10^{22} cm $^{-2}$)	$N_{H,2}$ (10^{22} cm $^{-2}$)	factor	R	C/ ν
00012178002	58803	31 $^{+3}_{-3}$	3.4 $^{+0.3}_{-0.3}$	0.33 $^{+0.02}_{-0.02}$	-0.6 $^{+0.2}_{-0.2}$	352/318 = 1.108
00012178003	58803	32 $^{+3}_{-3}$	1.9 $^{+0.4}_{-0.4}$	0.18 $^{+0.02}_{-0.02}$	-0.6 $^{+0.2}_{-0.2}$	213/216 = 0.987
00034292243a	58805	44 $^{+4}_{-4}$	4 $^{+1}_{-1}$	0.16 $^{+0.02}_{-0.02}$	-0.6 $^{+0.2}_{-0.2}$	196/165 = 1.189
00034292243b	58805	48 $^{+5}_{-4}$	5 $^{+1}_{-1}$	0.21 $^{+0.01}_{-0.02}$	0.0 $^{+0.0}_{-0.2}$	153/145 = 1.057
00012178004	58806	78 $^{+13}_{-11}$	6 $^{+1}_{-1}$	0.19 $^{+0.04}_{-0.03}$	-1.6 $^{+0.4}_{-0.4}$	70/73 = 0.969
00012178005	58806	65 $^{+12}_{-11}$	5.2 $^{+1.3}_{-1.3}$	0.19 $^{+0.04}_{-0.04}$	-0.4 $^{+0.4}_{-0.4}$	28/33 = 0.862
00012178006	58807	31 $^{+1}_{-1}$	2.9 $^{+0.2}_{-0.2}$	0.2 $^{+0.01}_{-0.01}$	-0.6 $^{+0.1}_{-0.1}$	598/542 = 1.104
00012178006 (flare)	58807	31 $^{+1}_{-1}$	3.3 $^{+0.2}_{-0.2}$	0.16 $^{+0.01}_{-0.01}$	-0.03 $^{+0.03}_{-0.07}$	733/685 = 1.071
00012178007	58808	28 $^{+3}_{-3}$	2 $^{+1}_{-1}$	0.19 $^{+0.03}_{-0.03}$	-3.7 $^{+0.4}_{-0.4}$	169/204 = 0.832
00012178008	58809	100 $^{+10}_{-10}$	5 $^{+1}_{-1}$	0.18 $^{+0.02}_{-0.02}$	-0.5 $^{+0.2}_{-0.2}$	122/110 = 1.111
00012178009	58810	35 $^{+4}_{-3}$	1.9 $^{+0.4}_{-0.4}$	0.19 $^{+0.02}_{-0.02}$	-0.9 $^{+0.3}_{-0.3}$	173/145 = 1.198
00012178011	58814	50 $^{+22}_{-22}$	0 $^{+4}_{-0}$	0.25 $^{+0.07}_{-0.03}$	0.0 $^{+0.0}_{-0.5}$	7/9 = 0.818
00012178012	58815	150 $^{+20}_{-20}$	9 $^{+1}_{-1}$	0.07 $^{+0.01}_{-0.02}$	-0.8 $^{+0.2}_{-0.2}$	51/51 = 1.017
00012178014	58816	69 $^{+6}_{-6}$	4 $^{+1}_{-1}$	0.17 $^{+0.02}_{-0.02}$	-1.8 $^{+0.2}_{-0.2}$	301/258 = 1.17
00012178015	58817	110 $^{+20}_{-20}$	0 $^{+4}_{-0}$	0.09 $^{+0.02}_{-0.02}$	-0.2 $^{+0.2}_{-0.2}$	23/13 = 1.78
00034292245a	58819	82 $^{+9}_{-8}$	5 $^{+1}_{-1}$	0.18 $^{+0.02}_{-0.02}$	-1.9 $^{+0.2}_{-0.3}$	217/165 = 1.317
00034292245b	58819	67 $^{+14}_{-12}$	6 $^{+2}_{-2}$	0.19 $^{+0.05}_{-0.04}$	-1.6 $^{+0.4}_{-0.5}$	63/52 = 1.227
00012178016	58819	36 $^{+4}_{-4}$	3 $^{+1}_{-1}$	0.2 $^{+0.02}_{-0.02}$	-3.3 $^{+0.3}_{-0.3}$	211/210 = 1.009
00012178017	58820	95 $^{+13}_{-12}$	6 $^{+2}_{-2}$	0.11 $^{+0.03}_{-0.03}$	-1.2 $^{+0.3}_{-0.3}$	85/73 = 1.165
00012178018	58821	34 $^{+5}_{-4}$	0.1 $^{+0.6}_{-0.1}$	0.09 $^{+0.02}_{-0.01}$	-1.2 $^{+0.4}_{-0.3}$	76/74 = 1.04
00012178019	58822	54 $^{+15}_{-11}$	10 $^{+2}_{-1}$	0.2 $^{+0.1}_{-0.1}$	-1.2 $^{+0.6}_{-0.6}$	24/20 = 1.234
00012178019 (flare)	58822	67 $^{+13}_{-12}$	3 $^{+2}_{-2}$	0.12 $^{+0.04}_{-0.04}$	-0.7 $^{+0.5}_{-0.5}$	24/29 = 0.836
00012178020	58823	78 $^{+11}_{-10}$	8 $^{+1}_{-1}$	0.16 $^{+0.03}_{-0.03}$	-1.3 $^{+0.3}_{-0.3}$	88/90 = 0.983
00012178021	58824	70 $^{+9}_{-8}$	7 $^{+1}_{-1}$	0.17 $^{+0.03}_{-0.03}$	-1.5 $^{+0.3}_{-0.3}$	160/132 = 1.214
00088850006	58897	93 $^{+15}_{-13}$	10 $^{+2}_{-1}$	0.1 $^{+0.03}_{-0.04}$	-3.1 $^{+0.4}_{-0.4}$	93/91 = 1.029
00088850005	58900	110 $^{+40}_{-30}$	10 $^{+10}_{-10}$	0.09 $^{+0.07}_{-0.05}$	-1.2 $^{+0.3}_{-0.3}$	20/24 = 0.87
00012178030	58920	58 $^{+27}_{-20}$	10 $^{+4}_{-4}$	0.4 $^{+0.1}_{-0.1}$	-1.9 $^{+0.8}_{-0.9}$	31/24 = 1.318
00012178031	58924	29 $^{+7}_{-6}$	4 $^{+1}_{-1}$	0.5 $^{+0.1}_{-0.1}$	-3.5 $^{+0.7}_{-0.8}$	97/105 = 0.927
00012178032	58927	11 $^{+10}_{-10}$	5 $^{+1}_{-1}$	0.19 $^{+0.02}_{-0.02}$	0.0 $^{+0.0}_{-0.2}$	56/47 = 1.192
00012178033	58930	26 $^{+5}_{-4}$	0.4 $^{+2.0}_{-0.4}$	0.1 $^{+0.05}_{-0.02}$	-3.1 $^{+0.7}_{-0.5}$	102/52 = 1.978
00012178034	58933	140 $^{+20}_{-20}$	3 $^{+6}_{-3}$	0.04 $^{+0.02}_{-0.02}$	-0.03 $^{+0.03}_{-0.18}$	6/7 = 0.889
00012178036a	58934	150 $^{+20}_{-20}$	9 $^{+3}_{-3}$	0.08 $^{+0.02}_{-0.02}$	-0.2 $^{+0.2}_{-0.2}$	19/27 = 0.737
00012178036b	58934	69 $^{+18}_{-15}$	5 $^{+1}_{-1}$	0.3 $^{+0.1}_{-0.1}$	-3.4 $^{+0.6}_{-0.6}$	93/75 = 1.251
00012178037 (flare)	58936	54 $^{+1}_{-1}$	0.9 $^{+0.3}_{-0.3}$	0.04 $^{+0.01}_{-0.01}$	-0.3 $^{+0.1}_{-0.1}$	583/526 = 1.109
00012178037	58936	71 $^{+3}_{-3}$	1.4 $^{+0.3}_{-0.3}$	0.09 $^{+0.01}_{-0.01}$	-0.8 $^{+0.1}_{-0.1}$	376/356 = 1.058
00012178038	58936	270 $^{+100}_{-50}$	1.1 $^{+0.2}_{-0.2}$	0.22 $^{+0.01}_{-0.01}$	-0.9 $^{+0.2}_{-0.2}$	163/153 = 1.07
00012178039	58937	410 $^{+170}_{-150}$	0 $^{+0.3}_{-0.0}$	0.2 $^{+0.02}_{-0.01}$	-0.6 $^{+0.2}_{-0.2}$	29/38 = 0.768
00012178040	58939	83 $^{+9}_{-8}$	0 $^{+0.4}_{-0.0}$	0.04 $^{+0.01}_{-0.0}$	-2.2 $^{+0.2}_{-0.2}$	130/109 = 1.195
00012178041	58940	65 $^{+12}_{-10}$	4 $^{+2}_{-2}$	0.13 $^{+0.04}_{-0.04}$	-1.6 $^{+0.4}_{-0.4}$	40/44 = 0.93
00012178042	58940	160 $^{+20}_{-20}$	3 $^{+4}_{-3}$	0.05 $^{+0.02}_{-0.02}$	-0.2 $^{+0.2}_{-0.2}$	14/14 = 1.009

Table 2 continued

Table 2 (*continued*)

OBSID	MJD	$N_{H,1}$	$N_{H,2}$	factor	R	C/ν
	(58000)	(10^{22} cm^{-2})	(10^{22} cm^{-2})			

NOTE—Continuum parameters. The table above lists the observation IDs, start time of observations (in units of MJD), column densities (in units of 10^{22} cm^{-2}), values of factor from the `const` component, and reflection fraction from the `pevxmon` component. The photon reflection fraction was constrained between and $-5 \leq R \leq 0$. Errors reported are 1σ errors.

Table 3. Flux related parameters

MJD	F_{central}	$F_{\text{scattering}}$	$F_{\text{reflection}}$	$F_{\text{unabsorbed}}$	Ratio	f_{Edd}	L
(58000)	($10^{-10} \frac{\text{erg}}{\text{cm}^2 \text{s}}$)	($10^{-11} \frac{\text{erg}}{\text{cm}^2 \text{s}}$)	($10^{-11} \frac{\text{erg}}{\text{cm}^2 \text{s}}$)	($10^{-9} \frac{\text{erg}}{\text{cm}^2 \text{s}}$)			(10^{37} erg/s)
58574	11 ⁺¹ ₋₁	78 ⁺⁴ ₋₄	1.4 ^{+0.1} _{-0.1} × 10 ⁻⁴	3.1 ^{+0.1} _{-0.2}	2.8 ^{+0.1} _{-0.1}	0.22 ^{+0.01} _{-0.01}	2.7 ^{+0.1} _{-0.1}
58596	11 ⁺¹ ₋₁	85 ⁺³ ₋₃	1.6 ^{+0.1} _{-0.1} × 10 ⁻⁴	2.9 ^{+0.1} _{-0.1}	2.6 ^{+0.1} _{-0.1}	0.20 ^{+0.01} _{-0.01}	2.6 ^{+0.1} _{-0.1}
58597	8.5 ^{+0.3} _{-0.3}	68 ⁺² ₋₂	1.4 ^{+0.1} _{-0.1} × 10 ⁻⁴	3.4 ^{+0.1} _{-0.1}	4.1 ^{+0.1} _{-0.1}	0.24 ^{+0.01} _{-0.01}	3.0 ^{+0.1} _{-0.1}
58611	2.8 ^{+0.1} _{-0.1}	25 ⁺¹ ₋₁	3.4 ^{+0.1} _{-0.1}	1.1 ^{+0.1} _{-0.1}	4.0 ^{+0.1} _{-0.1}	0.079 ^{+0.002} _{-0.002}	1.03 ^{+0.01} _{-0.01}
58612	3.7 ^{+0.1} _{-0.1}	24 ⁺¹ ₋₁	1.5 ^{+0.0} _{-0.0}	1.6 ^{+0.01} _{-0.01}	4.3 ^{+0.1} _{-0.1}	0.11 ^{+0.01} _{-0.01}	1.42 ^{+0.01} _{-0.01}
58613	2.6 ^{+0.1} _{-0.1}	23 ⁺¹ ₋₁	1.2 ^{+0.1} _{-0.1} × 10 ⁻³	1.1 ^{+1 × 10⁻³} _{-1 × 10⁻³}	4.1 ^{+0.2} _{-0.2}	0.075 ^{+0.003} _{-0.003}	0.90 ^{+0.01} _{-0.01}
58614	1.7 ^{+0.1} _{-0.1}	20 ⁺¹ ₋₁	2.4 ^{+0.1} _{-0.1}	0.62 ^{+0.01} _{-0.01}	3.7 ^{+0.2} _{-0.2}	0.044 ^{+0.002} _{-0.002}	0.63 ^{+0.01} _{-0.05}
58620	1.0 ^{+0.1} _{-0.1}	6.9 ^{+0.4} _{-0.4}	4.6 ^{+0.3} _{-0.3}	2.4 ^{+0.1} _{-0.1}	24 ⁺¹ ₋₁	0.17 ^{+0.01} _{-0.01}	2.1 ^{+0.1} _{-0.1}
58626	3.9 ^{+0.2} _{-0.2}	22 ⁺¹ ₋₁	3.2 ^{+0.1} _{-0.1}	3.3 ^{+0.1} _{-0.1}	8.4 ^{+0.3} _{-0.3}	0.23 ^{+0.01} _{-0.01}	2.9 ^{+0.1} _{-0.1}
58627	1.4 ^{+0.1} _{-0.1}	7.5 ^{+0.3} _{-0.3}	11 ⁺¹ ₋₁	0.900 ^{+0.003} _{-0.002}	6.6 ^{+0.3} _{-0.3}	0.066 ^{+0.002} _{-0.002}	0.85 ^{+0.01} _{-0.01}
58628	0.75 ^{+0.05} _{-0.05}	4.5 ^{+0.3} _{-0.3}	1.3 ^{+0.1} _{-0.1}	3.9 ^{+0.2} _{-0.2}	53 ⁺³ ₋₃	0.28 ^{+0.02} _{-0.02}	3.5 ^{+0.2} _{-0.2}
58630	2.1 ^{+0.1} _{-0.1}	3.9 ^{+0.1} _{-0.1}	16 ⁺¹ ₋₁	0.73 ^{+0.01} _{-0.01}	3.2 ^{+0.1} _{-0.1}	0.047 ^{+0.002} _{-0.002}	0.62 ^{+0.01} _{-0.01}
58630	0.8 ^{+0.1} _{-0.1}	5 ⁺¹ ₋₁	1.0 ^{+0.1} _{-0.1}	0.4 ^{+0.1} _{-0.1}	5.4 ^{+0.7} _{-0.7}	0.030 ^{+0.004} _{-0.004}	0.47 ^{+0.14} _{-0.01}
58632	1.7 ^{+0.1} _{-0.1}	14 ⁺¹ ₋₁	24 ⁺¹ ₋₁	2.0 ^{+0.1} _{-0.1}	12 ⁺¹ ₋₁	0.14 ^{+0.01} _{-0.01}	1.7 ^{+0.1} _{-0.1}
58633	0.4 ^{+0.1} _{-0.1}	0.8 ^{+0.2} _{-0.2}	0.21 ^{+0.01} _{-0.01}	0.26 ^{+0.01} _{-0.01}	4.7 ^{+1.2} _{-0.8}	0.012 ^{+0.003} _{-0.002}	0.192 ^{+0.001} _{-0.001}
58634	0.66 ^{+0.05} _{-0.05}	3.7 ^{+0.3} _{-0.3}	3.1 ^{+0.2} _{-0.2}	1.3 ^{+0.1} _{-0.1}	20 ⁺² ₋₂	0.091 ^{+0.007} _{-0.007}	1.2 ^{+0.1} _{-0.1}
58635	0.5 ^{+0.1} _{-0.1}	2.5 ^{+0.5} _{-0.6}	1.4 ^{+0.3} _{-0.4}	1.1 ^{+0.2} _{-0.3}	24 ⁺⁵ ₋₆	0.08 ^{+0.02} _{-0.02}	1.0 ^{+0.2} _{-0.2}
58635	1.4 ^{+0.1} _{-0.1}	3.1 ^{+0.2} _{-0.2}	5.0 ^{+0.3} _{-0.3}	0.8 ^{+0.1} _{-0.1}	6.1 ^{+0.4} _{-0.4}	0.059 ^{+0.004} _{-0.003}	0.7 ^{+0.1} _{-0.0}
58636	13 ^{+0.3} _{-0.3}	47 ⁺¹ ₋₁	32 ⁺¹ ₋₁	5.7 ^{+0.1} _{-0.1}	4.6 ^{+0.1} _{-0.1}	0.40 ^{+0.01} _{-0.01}	5.1 ^{+0.1} _{-0.1}
58638	7.9 ^{+0.4} _{-0.4}	38 ⁺² ₋₂	37 ⁺² ₋₂	3.3 ^{+0.2} _{-0.2}	4.1 ^{+0.2} _{-0.2}	0.23 ^{+0.01} _{-0.01}	2.9 ^{+0.1} _{-0.1}
58638	4.2 ^{+0.1} _{-0.1}	40 ⁺¹ ₋₁	26 ⁺¹ ₋₁	4.6 ^{+0.1} _{-0.1}	10.9 ^{+0.2} _{-0.3}	0.32 ^{+0.01} _{-0.01}	4.1 ^{+0.1} _{-0.1}
58639	2.9 ^{+0.3} _{-0.3}	14 ⁺¹ ₋₁	3.4 ^{+0.3} _{-0.3}	2.3 ^{+0.2} _{-0.2}	7.8 ^{+0.8} _{-0.7}	0.16 ^{+0.02} _{-0.02}	2.0 ^{+0.2} _{-0.2}
58640	4.3 ^{+0.2} _{-0.2}	5.4 ^{+0.3} _{-0.3}	29 ⁺² ₋₂	2.7 ^{+0.2} _{-0.1}	6.2 ^{+0.4} _{-0.3}	0.19 ^{+0.01} _{-0.01}	2.4 ^{+0.1} _{-0.1}
58641	1.6 ^{+0.1} _{-0.1}	4.1 ^{+0.2} _{-0.2}	12 ⁺¹ ₋₁	1.3 ^{+0.1} _{-0.1}	8.2 ^{+0.5} _{-0.5}	0.092 ^{+0.005} _{-0.005}	1.2 ^{+0.1} _{-0.1}
58642	1.8 ^{+0.1} _{-0.1}	5.9 ^{+0.5} _{-0.5}	5.2 ^{+0.4} _{-0.4}	1.1 ^{+0.1} _{-0.1}	7 ⁺¹ ₋₁	0.08 ^{+0.01} _{-0.01}	1.0 ^{+0.1} _{-0.1}
58643	2.3 ^{+0.1} _{-0.1}	33 ⁺² ₋₂	23 ⁺¹ ₋₁	4.5 ^{+0.2} _{-0.2}	20 ⁺¹ ₋₁	0.32 ^{+0.01} _{-0.02}	4.0 ^{+0.2} _{-0.2}
58643	2.7 ^{+0.3} _{-0.3}	11 ⁺¹ ₋₁	4.1 ^{+0.4} _{-0.4}	3.7 ^{+0.4} _{-0.4}	14 ⁺¹ ₋₁	0.26 ^{+0.03} _{-0.03}	3.3 ^{+0.3} _{-0.3}
58643	1.0 ^{+0.1} _{-0.1}	5.1 ^{+0.4} _{-0.4}	2.4 ^{+0.2} _{-0.2}	1.8 ^{+0.2} _{-0.2}	18 ⁺² ₋₂	0.13 ^{+0.01} _{-0.01}	1.6 ^{+0.1} _{-0.1}

Table 3 continued

Table 3 (continued)

MJD	F _{central}	F _{scattering}	F _{reflection}	F _{unabsorbed}	Ratio	f _{Edd}	L
(58000)	(10 ⁻¹⁰ $\frac{\text{erg}}{\text{cm}^2\text{s}}$)	(10 ⁻¹¹ $\frac{\text{erg}}{\text{cm}^2\text{s}}$)	(10 ⁻¹¹ $\frac{\text{erg}}{\text{cm}^2\text{s}}$)	(10 ⁻⁹ $\frac{\text{erg}}{\text{cm}^2\text{s}}$)			(10 ³⁷ erg/s)
58645	22 $^{+2}_{-2}$	150 $^{+10}_{-10}$	140 $^{+10}_{-10}$	22 $^{+2}_{-2}$	10 $^{+1}_{-1}$	1.5 $^{+0.1}_{-0.1}$	19 $^{+1}_{-2}$
58646	1400 $^{+90}_{-90}$	6700 $^{+400}_{-400}$	5100 $^{+300}_{-300}$	920 $^{+60}_{-60}$	6.7 $^{+0.4}_{-0.4}$	65 $^{+4}_{-4}$	810 $^{+50}_{-50}$
58653	2.6 $^{+0.1}_{-0.1}$	10 $^{+1}_{-1}$	10 $^{+1}_{-1}$	2.0 $^{+0.1}_{-0.1}$	7.9 $^{+0.5}_{-0.5}$	0.14 $^{+0.01}_{-0.01}$	1.8 $^{+0.1}_{-0.1}$
58658	51 $^{+5}_{-5}$	250 $^{+20}_{-20}$	160 $^{+10}_{-10}$	77 $^{+7}_{-7}$	15 $^{+1}_{-1}$	5 $^{+1}_{-1}$	68 $^{+6}_{-6}$
58660	1.0 $^{+0.1}_{-0.1}$	23 $^{+1}_{-1}$	14 $^{+1}_{-1}$	2.0 $^{+0.1}_{-0.1}$	20 $^{+1}_{-1}$	0.14 $^{+0.01}_{-0.01}$	1.8 $^{+0.1}_{-0.1}$
58662	1.8 $^{+0.1}_{-0.1}$	4.0 $^{+0.3}_{-0.3}$	11 $^{+1}_{-1}$	1.0 $^{+0.1}_{-0.1}$	5.9 $^{+0.5}_{-0.4}$	0.07 $^{+0.01}_{-0.01}$	0.9 $^{+0.1}_{-0.1}$
58662	1.9 $^{+0.1}_{-0.1}$	17 $^{+1}_{-1}$	21 $^{+1}_{-1}$	2.3 $^{+0.1}_{-0.1}$	12 $^{+1}_{-1}$	0.16 $^{+0.01}_{-0.01}$	2.0 $^{+0.1}_{-0.1}$
58662	2.9 $^{+0.3}_{-0.2}$	16 $^{+2}_{-1}$	23 $^{+2}_{-2}$	1.8 $^{+0.2}_{-0.2}$	6 $^{+1}_{-1}$	0.13 $^{+0.01}_{-0.01}$	1.6 $^{+0.1}_{-0.1}$
58675	1.4 $^{+0.1}_{-0.1}$	10 $^{+1}_{-1}$	11 $^{+1}_{-1}$	4.5 $^{+0.3}_{-0.3}$	32 $^{+2}_{-2}$	0.32 $^{+0.02}_{-0.02}$	4.0 $^{+0.2}_{-0.2}$
58676	0.54 $^{+0.05}_{-0.05}$	3.1 $^{+0.3}_{-0.3}$	10 $^{+1}_{-1}$	0.7 $^{+0.1}_{-0.1}$	13 $^{+1}_{-1}$	0.049 $^{+0.004}_{-0.005}$	0.6 $^{+0.1}_{-0.1}$
58678	0.4 $^{+0.1}_{-0.1}$	5 $^{+1}_{-1}$	7 $^{+1}_{-1}$	1.5 $^{+0.3}_{-0.2}$	37 $^{+6}_{-5}$	0.10 $^{+0.02}_{-0.02}$	1.3 $^{+0.2}_{-0.2}$
58679	1.5 $^{+0.1}_{-0.1}$	13 $^{+1}_{-1}$	12 $^{+1}_{-1}$	1.6 $^{+0.1}_{-0.1}$	11 $^{+1}_{-1}$	0.11 $^{+0.01}_{-0.01}$	1.4 $^{+0.1}_{-0.1}$
58679	0.63 $^{+0.01}_{-0.01}$	6.2 $^{+0.4}_{-0.3}$	1.3 $^{+0.1}_{-0.1}$	2.4 $^{+0.1}_{-0.1}$	37 $^{+2}_{-2}$	0.17 $^{+0.01}_{-0.01}$	2.1 $^{+0.1}_{-0.1}$
58680	0.8 $^{+0.1}_{-0.1}$	5.8 $^{+0.4}_{-0.4}$	1.6 $^{+0.1}_{-0.1}$	2.8 $^{+0.2}_{-0.2}$	35 $^{+2}_{-2}$	0.20 $^{+0.01}_{-0.01}$	2.5 $^{+0.2}_{-0.2}$
58682	0.57 $^{+0.01}_{-0.01}$	2.8 $^{+0.2}_{-0.3}$	4.3 $^{+0.4}_{-0.4}$	0.54 $^{+0.01}_{-0.01}$	11 $^{+1}_{-1}$	0.038 $^{+0.003}_{-0.003}$	0.53 $^{+0.01}_{-0.01}$
58683	0.56 $^{+0.01}_{-0.01}$	3.2 $^{+0.2}_{-0.2}$	6.6 $^{+0.5}_{-0.5}$	0.76 $^{+0.01}_{-0.01}$	14 $^{+1}_{-1}$	0.048 $^{+0.003}_{-0.003}$	0.60 $^{+0.01}_{-0.01}$
58684	1.1 $^{+0.1}_{-0.1}$	16 $^{+1}_{-1}$	10 $^{+1}_{-1}$	1.7 $^{+0.1}_{-0.1}$	15 $^{+1}_{-1}$	0.12 $^{+0.01}_{-0.01}$	1.5 $^{+0.1}_{-0.1}$
58690	2.9 $^{+0.3}_{-0.2}$	16 $^{+2}_{-1}$	23 $^{+2}_{-2}$	1.8 $^{+0.2}_{-0.2}$	6 $^{+1}_{-1}$	0.13 $^{+0.01}_{-0.01}$	1.6 $^{+0.1}_{-0.1}$
58690	1.4 $^{+0.1}_{-0.1}$	9.8 $^{+0.6}_{-0.6}$	11 $^{+1}_{-1}$	4.5 $^{+0.3}_{-0.3}$	32 $^{+2}_{-2}$	0.32 $^{+0.02}_{-0.02}$	4.0 $^{+0.2}_{-0.2}$
58692	1.2 $^{+0.2}_{-0.2}$	1.2 $^{+0.2}_{-0.2}$	2.7 $^{+0.5}_{-0.4}$	0.9 $^{+0.2}_{-0.1}$	7 $^{+1}_{-1}$	0.060 $^{+0.011}_{-0.009}$	0.8 $^{+0.1}_{-0.1}$
58692	2.3 $^{+0.1}_{-0.1}$	5.8 $^{+0.3}_{-0.3}$	12 $^{+1}_{-1}$	1.9 $^{+0.1}_{-0.1}$	9 $^{+1}_{-1}$	0.14 $^{+0.01}_{-0.01}$	1.7 $^{+0.1}_{-0.1}$
58694	0.98 $^{+0.01}_{-0.1}$	5.2 $^{+0.3}_{-0.3}$	8 $^{+1}_{-1}$	0.69 $^{+0.01}_{-0.01}$	9 $^{+1}_{-1}$	0.052 $^{+0.003}_{-0.003}$	0.72 $^{+0.01}_{-0.01}$
58694	3.6 $^{+0.4}_{-0.3}$	10 $^{+1}_{-1}$	11 $^{+1}_{-1}$	1.9 $^{+0.2}_{-0.2}$	5 $^{+1}_{-1}$	0.13 $^{+0.01}_{-0.01}$	1.7 $^{+0.2}_{-0.2}$
58695	2.1 $^{+0.2}_{-0.2}$	7 $^{+1}_{-1}$	15 $^{+1}_{-1}$	1.9 $^{+0.1}_{-0.1}$	9 $^{+1}_{-1}$	0.13 $^{+0.01}_{-0.01}$	1.7 $^{+0.1}_{-0.1}$
58723	3.2 $^{+0.2}_{-0.2}$	20 $^{+1}_{-1}$	11 $^{+1}_{-1}$	2.1 $^{+0.1}_{-0.1}$	6.8 $^{+0.4}_{-0.4}$	0.15 $^{+0.01}_{-0.01}$	1.9 $^{+0.1}_{-0.1}$
58725	1.2 $^{+0.1}_{-0.1}$	8 $^{+1}_{-1}$	3.8 $^{+0.4}_{-0.4}$	0.8 $^{+0.1}_{-0.1}$	7 $^{+1}_{-1}$	0.06 $^{+0.01}_{-0.01}$	0.7 $^{+0.1}_{-0.1}$
58728	0.7 $^{+0.1}_{-0.1}$	6 $^{+1}_{-1}$	6 $^{+1}_{-1}$	0.9 $^{+0.1}_{-0.1}$	13 $^{+1}_{-1}$	0.07 $^{+0.01}_{-0.01}$	0.8 $^{+0.1}_{-0.1}$
58730	2.5 $^{+0.1}_{-0.1}$	19 $^{+1}_{-1}$	14 $^{+1}_{-1}$	3.1 $^{+0.2}_{-0.2}$	13 $^{+1}_{-1}$	0.22 $^{+0.01}_{-0.01}$	2.8 $^{+0.2}_{-0.2}$
58732	1.0 $^{+0.1}_{-0.1}$	5 $^{+1}_{-1}$	1.0 $^{+0.1}_{-0.1}$	2.1 $^{+0.3}_{-0.3}$	22 $^{+3}_{-3}$	0.15 $^{+0.02}_{-0.02}$	1.9 $^{+0.3}_{-0.3}$
58733	1.5 $^{+0.1}_{-0.1}$	14 $^{+1}_{-1}$	16 $^{+1}_{-1}$	1.6 $^{+0.1}_{-0.1}$	11 $^{+1}_{-1}$	0.11 $^{+0.01}_{-0.01}$	1.4 $^{+0.1}_{-0.1}$
58734	0.9 $^{+0.1}_{-0.1}$	6.1 $^{+0.4}_{-0.4}$	10 $^{+1}_{-1}$	0.9 $^{+0.1}_{-0.1}$	10 $^{+1}_{-1}$	0.063 $^{+0.004}_{-0.004}$	0.84 $^{+0.01}_{-0.01}$
58734	1.5 $^{+0.1}_{-0.1}$	4.4 $^{+0.4}_{-0.4}$	5.5 $^{+0.6}_{-0.5}$	2.2 $^{+0.2}_{-0.2}$	15 $^{+2}_{-2}$	0.16 $^{+0.02}_{-0.02}$	2.0 $^{+0.2}_{-0.2}$
58735	1.0 $^{+0.4}_{-0.4}$	7 $^{+3}_{-3}$	0.004 $^{+0.001}_{-0.002}$	1.1 $^{+0.4}_{-0.5}$	11 $^{+4}_{-5}$	0.08 $^{+0.03}_{-0.03}$	1.0 $^{+0.4}_{-0.4}$
58742	2.0 $^{+0.2}_{-0.2}$	6 $^{+1}_{-1}$	4 $^{+1}_{-1}$	1.7 $^{+0.2}_{-0.2}$	9 $^{+1}_{-1}$	0.12 $^{+0.01}_{-0.01}$	1.5 $^{+0.2}_{-0.2}$
58744	1.9 $^{+0.1}_{-0.1}$	14 $^{+1}_{-1}$	6.2 $^{+0.5}_{-0.4}$	3.5 $^{+0.3}_{-0.3}$	18 $^{+1}_{-1}$	0.25 $^{+0.02}_{-0.02}$	3.1 $^{+0.2}_{-0.2}$
58746	3.2 $^{+0.2}_{-0.2}$	3.8 $^{+0.3}_{-0.2}$	12 $^{+1}_{-1}$	1.4 $^{+0.1}_{-0.1}$	4.5 $^{+0.3}_{-0.3}$	0.10 $^{+0.01}_{-0.01}$	1.3 $^{+0.1}_{-0.1}$
58748	0.37 $^{+0.02}_{-0.03}$	5.7 $^{+0.4}_{-0.4}$	15.9 $^{+1.0}_{-1.1}$	0.9 $^{+0.1}_{-0.1}$	22.78 $^{+1.48}_{-1.62}$	0.060 $^{+0.004}_{-0.004}$	0.8 $^{+0.0}_{-0.1}$
58748	0.29 $^{+0.02}_{-0.02}$	4.7 $^{+0.3}_{-0.3}$	9 $^{+1}_{-1}$	19 $^{+1}_{-1}$	640 $^{+40}_{-40}$	1.3 $^{+0.1}_{-0.1}$	16 $^{+1}_{-1}$
58750	2.8 $^{+0.2}_{-0.2}$	4.7 $^{+0.3}_{-0.3}$	9 $^{+1}_{-1}$	19 $^{+1}_{-1}$	69 $^{+4}_{-4}$	1.4 $^{+0.1}_{-0.1}$	17 $^{+1}_{-1}$
58751	4.4 $^{+0.2}_{-0.2}$	28 $^{+1}_{-1}$	36 $^{+2}_{-2}$	2.4 $^{+0.1}_{-0.1}$	5.5 $^{+0.3}_{-0.3}$	0.17 $^{+0.01}_{-0.01}$	2.1 $^{+0.1}_{-0.1}$

Table 3 continued

Table 3 (continued)

MJD	F _{central}	F _{scattering}	F _{reflection}	F _{unabsorbed}	Ratio	f _{Edd}	L
(58000)	(10 ⁻¹⁰ $\frac{\text{erg}}{\text{cm}^2\text{s}}$)	(10 ⁻¹¹ $\frac{\text{erg}}{\text{cm}^2\text{s}}$)	(10 ⁻¹¹ $\frac{\text{erg}}{\text{cm}^2\text{s}}$)	(10 ⁻⁹ $\frac{\text{erg}}{\text{cm}^2\text{s}}$)			(10 ³⁷ erg/s)
58752	3.2 ^{+0.2} _{-0.2}	12 ⁺¹ ₋₁	19 ⁺¹ ₋₁	1.7 ^{+0.1} _{-0.1}	5.4 ^{+0.4} _{-0.3}	0.12 ^{+0.01} _{-0.01}	1.5 ^{+0.1} _{-0.1}
58753	3.0 ^{+0.2} _{-0.2}	11 ⁺¹ ₋₁	24 ⁺² ₋₂	1.8 ^{+0.1} _{-0.1}	5.9 ^{+0.4} _{-0.4}	0.12 ^{+0.01} _{-0.01}	1.6 ^{+0.1} _{-0.1}
58753	4.2 ^{+0.2} _{-0.2}	18 ⁺¹ ₋₁	16.7 ^{+0.9} _{-0.9}	3.8 ^{+0.2} _{-0.2}	9 ⁺¹ ₋₁	0.26 ^{+0.01} _{-0.01}	3.3 ^{+0.2} _{-0.2}
58769	0.7 ^{+0.1} _{-0.1}	6.5 ^{+0.5} _{-0.5}	3.2 ^{+0.3} _{-0.3}	2.9 ^{+0.2} _{-0.2}	41 ⁺³ ₋₃	0.20 ^{+0.02} _{-0.02}	2.5 ^{+0.2} _{-0.2}
58769	1.5 ^{+0.1} _{-0.1}	2.2 ^{+0.2} _{-0.2}	8.0 ^{+0.7} _{-0.6}	0.8 ^{+0.1} _{-0.1}	5.1 ^{+0.5} _{-0.4}	0.054 ^{+0.005} _{-0.004}	0.7 ^{+0.1} _{-0.1}
58770	0.59 ^{+0.05} _{-0.05}	7 ⁺¹ ₋₁	4.2 ^{+0.3} _{-0.4}	0.7 ^{+0.1} _{-0.1}	11 ⁺¹ ₋₁	0.047 ^{+0.003} _{-0.002}	0.63 ^{+0.01} _{-0.14}
58773	0.4 ^{+0.1} _{-0.1}	2.6 ^{+0.5} _{-0.5}	3.2 ^{+0.6} _{-0.6}	0.7 ^{+0.1} _{-0.1}	16 ⁺³ ₋₃	0.048 ^{+0.009} _{-0.009}	0.6 ^{+0.1} _{-0.1}
58784	0.9 ^{+0.1} _{-0.1}	2.2 ^{+0.2} _{-0.1}	7.7 ^{+0.5} _{-0.5}	0.38 ^{+0.03} _{-0.02}	4.3 ^{+0.3} _{-0.3}	0.026 ^{+0.002} _{-0.002}	0.28 ^{+0.01} _{-0.02}
58798	1.5 ^{+0.1} _{-0.1}	9.1 ^{+0.5} _{-0.5}	11 ⁺¹ ₋₁	0.58 ^{+0.03} _{-0.03}	3.97 ^{+0.24} _{-0.22}	0.040 ^{+0.002} _{-0.002}	0.5 ^{+0.0} _{-0.0}
58801	3.9 ^{+0.2} _{-0.2}	14 ⁺¹ ₋₁	10.7 ^{+0.4} _{-0.4}	2.1 ^{+0.1} _{-0.1}	5.4 ^{+0.2} _{-0.2}	0.15 ^{+0.01} _{-0.01}	1.8 ^{+0.1} _{-0.1}
58803	5.8 ^{+0.2} _{-0.2}	12 ⁺¹ ₋₁	7.9 ^{+0.3} _{-0.3}	1.7 ^{+0.1} _{-0.1}	2.9 ^{+0.1} _{-0.1}	0.12 ^{+0.01} _{-0.01}	1.5 ^{+0.1} _{-0.1}
58803	8.8 ^{+0.4} _{-0.4}	4.2 ^{+0.2} _{-0.2}	1.2 ^{+0.1} _{-0.1}	0.55 ^{+0.03} _{-0.03}	0.63 ^{+0.03} _{-0.03}	0.039 ^{+0.002} _{-0.002}	0.52 ^{+0.03} _{-0.03}
58805	5.8 ^{+0.3} _{-0.3}	14 ⁺¹ ₋₁	9.9 ^{+0.6} _{-0.5}	2.1 ^{+0.1} _{-0.1}	3.7 ^{+0.2} _{-0.2}	0.15 ^{+0.01} _{-0.01}	1.9 ^{+0.1} _{-0.1}
58805	6.1 ^{+0.4} _{-0.4}	29 ⁺² ₋₂	6.0 ^{+0.4} _{-0.3}	2.0 ^{+0.1} _{-0.1}	3.2 ^{+0.2} _{-0.2}	0.14 ^{+0.01} _{-0.01}	1.8 ^{+0.1} _{-0.1}
58806	1.4 ^{+0.1} _{-0.1}	11 ⁺¹ ₋₁	10 ⁺¹ ₋₁	1.4 ^{+0.1} _{-0.1}	9.7 ^{+0.7} _{-0.7}	0.096 ^{+0.007} _{-0.007}	1.2 ^{+0.1} _{-0.1}
58806	0.7 ^{+0.1} _{-0.1}	4.2 ^{+0.4} _{-0.4}	1.2 ^{+0.1} _{-0.1}	0.5 ^{+0.1} _{-0.1}	8.1 ^{+0.9} _{-0.9}	0.039 ^{+0.004} _{-0.003}	0.48 ^{+0.1} _{-0.04}
58807	25 ^{+0.6} _{-0.6}	16.4 ^{+0.4} _{-0.4}	9.1 ^{+0.2} _{-0.2}	1.94 ^{+0.05} _{-0.04}	0.77 ^{+0.02} _{-0.02}	0.14 ^{+0.01} _{-0.01}	1.71 ^{+0.05} _{-0.04}
58807	140 ⁺² ₋₂	14.3 ^{+0.2} _{-0.2}	4.2 ^{+0.1} _{-0.1}	1.89 ^{+0.03} _{-0.03}	0.135 ^{+0.002} _{-0.002}	0.13 ^{+0.01} _{-0.01}	1.672 ^{+0.002} _{-0.002}
58808	2.9 ^{+0.1} _{-0.1}	11 ⁺¹ ₋₁	22 ⁺¹ ₋₁	1.3 ^{+0.1} _{-0.1}	4.4 ^{+0.2} _{-0.2}	0.089 ^{+0.004} _{-0.004}	1.49 ^{+0.07} _{-0.06}
58809	3.0 ^{+0.1} _{-0.1}	3.2 ^{+0.1} _{-0.1}	1.08 ^{+0.05} _{-0.05} × 10 ⁻⁵	0.2 ^{+0.0} _{-0.0}	0.77 ^{+0.04} _{-0.04}	0.016 ^{+0.007} _{-0.008}	0.27 ^{+0.01} _{-0.01}
58810	3.3 ^{+0.2} _{-0.2}	4.6 ^{+0.3} _{-0.2}	6.1 ^{+0.3} _{-0.3}	1.7 ^{+0.1} _{-0.1}	5.27 ^{+0.28} _{-0.27}	0.12 ^{+0.01} _{-0.01}	1.5 ^{+0.1} _{-0.1}
58814	0.4 ^{+0.1} _{-0.1}	3.2 ^{+0.7} _{-0.9}	1.1 ^{+0.3} _{-0.1} × 10 ⁻⁵	0.2 ^{+0.1} _{-0.1}	6 ⁺¹ ₋₂	0.017 ^{+0.004} _{-0.005}	0.27 ^{+0.01} _{-0.01}
58815	1.5 ^{+0.1} _{-0.1}	2.8 ^{+0.2} _{-0.2}	0.62 ^{+0.04} _{-0.04}	0.57 ^{+0.04} _{-0.04}	3.8 ^{+0.3} _{-0.3}	0.040 ^{+0.003} _{-0.003}	0.067 ^{+0.04} _{-0.04}
58816	3.1 ^{+0.1} _{-0.1}	19 ⁺¹ ₋₁	23 ⁺¹ ₋₁	2.6 ^{+0.1} _{-0.1}	8.5 ^{+0.3} _{-0.3}	0.19 ^{+0.01} _{-0.01}	2.3 ^{+0.1} _{-0.1}
58817	0.4 ^{+0.1} _{-0.1}	2.8 ^{+0.4} _{-0.4}	0.6 ^{+0.1} _{-0.1}	0.6 ^{+0.1} _{-0.1}	14.3 ^{+2.2} _{-2.2}	0.041 ^{+0.006} _{-0.007}	0.5 ^{+0.1} _{-0.1}
58819	2.1 ^{+0.1} _{-0.1}	9.8 ^{+0.4} _{-0.4}	17 ⁺¹ ₋₁	1.07 ^{+0.05} _{-0.06}	5.1 ^{+0.2} _{-0.2}	0.0875 ^{+0.004} _{-0.003}	0.92 ^{+0.01} _{-0.01}
58820	0.8 ^{+0.1} _{-0.1}	4.3 ^{+0.3} _{-0.3}	5.8 ^{+0.4} _{-0.4}	1.0 ^{+0.1} _{-0.1}	12.1 ^{+0.9} _{-0.9}	0.070 ^{+0.005} _{-0.004}	0.9 ^{+0.1} _{-0.1}
58821	1.1 ^{+0.1} _{-0.1}	2.8 ^{+0.2} _{-0.2}	3.0 ^{+0.2} _{-0.2}	0.6 ^{+0.0} _{-0.0}	4.9 ^{+0.4} _{-0.4}	0.040 ^{+0.003} _{-0.002}	0.45 ^{+0.03} _{-0.04}
58822	1.6 ^{+0.2} _{-0.2}	7.1 ^{+1.1} _{-1.0}	6.0 ^{+0.9} _{-0.8}	1.1 ^{+0.2} _{-0.1}	7 ⁺¹ ₋₁	0.077 ^{+0.011} _{-0.011}	1.0 ^{+0.1} _{-0.1}
58822	0.5 ^{+0.1} _{-0.1}	2.5 ^{+0.3} _{-0.3}	1.4 ^{+0.2} _{-0.2}	0.4 ^{+0.1} _{-0.1}	8 ⁺¹ ₋₁	0.031 ^{+0.004} _{-0.004}	0.52 ^{+0.06} _{-0.06}
58823	1.3 ^{+0.1} _{-0.1}	7.7 ^{+0.5} _{-0.5}	8 ⁺¹ ₋₁	1.3 ^{+0.1} _{-0.1}	9.7 ^{+0.7} _{-0.7}	0.091 ^{+0.006} _{-0.006}	1.2 ^{+0.1} _{-0.1}
58824	1.8 ^{+0.1} _{-0.1}	10 ⁺¹ ₋₁	11 ⁺¹ ₋₁	1.5 ^{+0.1} _{-0.1}	8.7 ^{+0.5} _{-0.5}	0.11 ^{+0.01} _{-0.01}	1.4 ^{+0.1} _{-0.1}
58897	0.76 ^{+0.05} _{-0.05}	3.1 ^{+0.2} _{-0.2}	13 ⁺¹ ₋₁	0.9 ^{+0.1} _{-0.1}	12 ⁺¹ ₋₁	0.063 ^{+0.004} _{-0.004}	1.05 ^{+0.06} _{-0.05}
58900	0.8 ^{+0.1} _{-0.2}	4 ⁺¹ ₋₁	6 ⁺¹ ₋₁	1.1 ^{+0.2} _{-0.2}	14 ⁺² ₋₃	0.079 ^{+0.015} _{-0.017}	1.0 ^{+0.2} _{-0.2}
58920	0.4 ^{+0.1} _{-0.1}	4 ⁺¹ ₋₁	2.4 ^{+0.4} _{-0.4}	0.28 ^{+0.04} _{-0.05}	7 ⁺¹ ₋₁	0.020 ^{+0.003} _{-0.003}	0.33 ^{+0.05} _{-0.05}
58924	0.8 ^{+0.1} _{-0.1}	8 ⁺¹ ₋₁	6.1 ^{+0.4} _{-0.4}	0.38 ^{+0.03} _{-0.03}	4.5 ^{+0.3} _{-0.3}	0.026 ^{+0.002} _{-0.002}	0.45 ^{+0.03} _{-0.03}
58927	0.64 ^{+0.04} _{-0.04}	7.7 ^{+0.5} _{-0.5}	1.4 ^{+0.09} _{-0.09} × 10 ⁻⁴	0.9 ^{+0.1} _{-0.1}	13 ⁺¹ ₋₁	0.060 ^{+0.004} _{-0.003}	1.02 ^{+0.06} _{-0.06}
58930	0.7 ^{+0.1} _{-0.1}	1.7 ^{+0.1} _{-0.1}	4.6 ^{+0.4} _{-0.4}	0.33 ^{+0.03} _{-0.03}	4.24 ^{+0.36} _{-0.33}	0.022 ^{+0.002} _{-0.002}	1.39 ^{+0.02} _{-0.02}
58933	0.6 ^{+0.1} _{-0.1}	2.2 ^{+0.4} _{-0.4}	0.18 ^{+0.02} _{-0.02}	1.2 ^{+0.2} _{-0.2}	21 ⁺⁴ ₋₄	0.083 ^{+0.014} _{-0.013}	1.0 ^{+0.2} _{-0.2}
58934	1.5 ^{+0.1} _{-0.1}	9.7 ^{+0.9} _{-0.9}	2.8 ^{+0.3} _{-0.3}	3.5 ^{+0.3} _{-0.3}	24 ⁺² ₋₂	0.25 ^{+0.02} _{-0.02}	3.1 ^{+0.3} _{-0.3}

Table 3 continued

Table 3 (*continued*)

MJD	F_{central}	$F_{\text{scattering}}$	$F_{\text{reflection}}$	$F_{\text{unabsorbed}}$	Ratio	f_{Edd}	L
(58000)	$(10^{-10} \frac{\text{erg}}{\text{cm}^2\text{s}})$	$(10^{-11} \frac{\text{erg}}{\text{cm}^2\text{s}})$	$(10^{-11} \frac{\text{erg}}{\text{cm}^2\text{s}})$	$(10^{-9} \frac{\text{erg}}{\text{cm}^2\text{s}})$			(10^{37} erg/s)
58934	0.57 ^{+0.04} _{-0.04}	6.1 ^{+0.4} _{-0.4}	7.9 ^{+0.5} _{-0.6}	0.48 ^{+0.03} _{-0.03}	8.5 ^{+0.6} _{-0.6}	0.034 ^{+0.002} _{-0.002}	0.57 ^{+0.06} _{-0.06}
58936	40 ⁺¹ ₋₁	52 ⁺¹ ₋₁	37 ⁺¹ ₋₁	28 ⁺¹ ₋₁	6.9 ^{+0.2} _{-0.2}	1.9 ^{+0.1} _{-0.1}	24 ⁺¹ ₋₁
58936	11 ^{+0.3} _{-0.3}	44 ⁺¹ ₋₁	36 ⁺¹ ₋₁	9.8 ^{+0.3} _{-0.3}	8.9 ^{+0.3} _{-0.3}	0.69 ^{+0.02} _{-0.02}	8.7 ^{+0.3} _{-0.2}
58936	0.192 ^{+0.005} _{-0.005}	18.5 ^{+0.4} _{-0.4}	6.8 ^{+0.2} _{-0.2}	1.58 ^{+0.07} _{-0.06}	87 ⁺² ₋₂	0.12 ^{+0.01} _{-0.01}	1.95 ^{+0.05} _{-0.05}
58937	0.80 ^{+0.03} _{-0.03}	0.96 ^{+0.04} _{-0.04}	0.75 ^{+0.03} _{-0.03}	0.160 ^{+0.007} _{-0.007}	1.99 ^{+0.08} _{-0.08}	0.011 ^{+0.005} _{-0.005}	0.19 ^{+0.01} _{-0.01}
58939	1.4 ^{+0.1} _{-0.1}	3.0 ^{+0.2} _{-0.2}	15 ⁺¹ ₋₁	1.5 ^{+0.1} _{-0.1}	10 ⁺¹ ₋₁	0.102 ^{+0.005} _{-0.006}	1.3 ^{+0.1} _{-0.1}
58940	1.5 ^{+0.1} _{-0.1}	7.0 ^{+0.6} _{-0.6}	8.6 ^{+0.8} _{-0.8}	1.2 ^{+0.1} _{-0.1}	8.1 ^{+0.7} _{-0.7}	0.083 ^{+0.008} _{-0.007}	1.0 ^{+0.1} _{-0.1}
58940	0.6 ^{+0.1} _{-0.1}	3.0 ^{+0.3} _{-0.3}	1.4 ^{+0.2} _{-0.1}	1.5 ^{+0.2} _{-0.2}	26 ⁺³ ₋₃	0.10 ^{+0.01} _{-0.01}	1.3 ^{+0.1} _{-0.1}

NOTE—Flux-related parameters. The table above lists the start time of observations (in units of MJD), the flux of the different components, the unabsorbed flux of the central engine, $F_{\text{unabsorbed}}/F_{\text{absorbed}}$, Eddington fraction, and source luminosity. The central engine flux, scattered flux, and reflected flux are in units of $10^{-10} \text{ erg cm}^{-2} \text{ s}^{-1}$, $10^{-11} \text{ erg cm}^{-2} \text{ s}^{-1}$, and $10^{-11} \text{ erg cm}^{-2} \text{ s}^{-1}$ respectively. The luminosity is reported in units of $10^{37} \text{ erg s}^{-1}$. Errors reported are 1σ errors.

Table 4. Flare Spectral Parameters

Flux Level	MJD	$N_{H,1}$ (10^{22} cm $^{-2}$)	$N_{H,2}$ (10^{22} cm $^{-2}$)	R	C/nu	F_{abs} (10^{-10} $\frac{\text{erg}}{\text{cm}^2\text{s}}$)	F_{unabs} (10^{-9} $\frac{\text{erg}}{\text{cm}^2\text{s}}$)	f_{Edd}
flare 1	high	26 $^{+3}_{-4}$	3 $^{+1}_{-1}$	-0.1 $^{+0.4}_{-0.4}$	322/331 = 0.974	180 $^{+10}_{-20}$	77 $^{+4}_{-6}$	7 $^{+1}_{-1}$
	med	30 $^{+4}_{-4}$	4 $^{+1}_{-1}$	-0.1 $^{+0.4}_{-0.4}$	264/284 = 0.932	140 $^{+10}_{-10}$	59 $^{+4}_{-5}$	6 $^{+1}_{-1}$
	low	34 $^{+3}_{-3}$	1 $^{+1}_{-1}$	0.0 $^{+0.0}_{-0.1}$	145/117 = 1.247	98 $^{+6}_{-7}$	48 $^{+3}_{-3}$	5 $^{+1}_{-1}$
flare 2	high	22 $^{+3}_{-3}$	1 $^{+1}_{-1}$	-0.7 $^{+0.4}_{-0.7}$	270/217 = 1.249	170 $^{+20}_{-20}$	67 $^{+6}_{-5}$	6 $^{+1}_{-1}$
	med	29 $^{+3}_{-3}$	3 $^{+1}_{-1}$	0.0 $^{+0.2}_{-0.2}$	247/282 = 0.877	140 $^{+10}_{-10}$	65 $^{+3}_{-3}$	6 $^{+0.3}_{-0.3}$
	low	24 $^{+4}_{-3}$	4 $^{+1}_{-1}$	0.0 $^{+0.0}_{-0.3}$	182/174 = 1.048	120 $^{+4}_{-4}$	49 $^{+2}_{-4}$	4.6 $^{+0.2}_{-0.3}$
flare3	high	35 $^{+7}_{-7}$	6.8 $^{+1.4}_{-1.3}$	-0.8 $^{+0.6}_{-0.8}$	153/152 = 1.009	84 $^{+15}_{-7}$	42 $^{+7}_{-4}$	3.9 $^{+0.7}_{-0.4}$
	med	40 $^{+5}_{-5}$	5.9 $^{+1.3}_{-1.3}$	0.0 $^{+0.0}_{-0.1}$	190/149 = 1.28	79 $^{+7}_{-5}$	43 $^{+3}_{-3}$	4.1 $^{+0.3}_{-0.3}$
	low	22 $^{+2}_{-2}$	1.2 $^{+1.5}_{-1.2}$	-0.01 $^{+0.03}_{-0.46}$	153/137 = 1.119	70 $^{+3}_{-6}$	27 $^{+2}_{-2}$	2.5 $^{+0.1}_{-0.2}$
flare 1	high	70 $^{+8}_{-7}$	0.8 $^{+1.5}_{-0.8}$	0.0 $^{+0.0}_{-0.3}$	20/31 = 0.652	130 $^{+10}_{-20}$	110 $^{+10}_{-20}$	11 $^{+1}_{-1}$
	med	60 $^{+8}_{-7}$	1.7 $^{+2.1}_{-1.7}$	-0.3 $^{+0.3}_{-0.6}$	52/43 = 1.215	44 $^{+9}_{-8}$	33 $^{+7}_{-6}$	3.1 $^{+0.7}_{-0.6}$
	low	62 $^{+12}_{-9}$	0.0 $^{+0.0}_{-0.8}$	-0.8 $^{+0.7}_{-0.8}$	33/19 = 1.741	20 $^{+3}_{-3}$	15 $^{+3}_{-2}$	1.4 $^{+0.3}_{-0.2}$
flare 2	high	65 $^{+13}_{-11}$	5 $^{+5}_{-5}$	-0.1 $^{+0.1}_{-0.7}$	15/24 = 0.662	120 $^{+20}_{-30}$	100 $^{+20}_{-20}$	9.3 $^{+1.7}_{-2.3}$
	med	54 $^{+8}_{-6}$	0.5 $^{+1.5}_{-0.5}$	-0.1 $^{+0.1}_{-0.6}$	50/34 = 1.484	49 $^{+7}_{-9}$	34 $^{+5}_{-6}$	3.1 $^{+0.5}_{-0.6}$
	low	65 $^{+11}_{-9}$	0.001 $^{+1.949}_{-0.001}$	-0.8 $^{+0.6}_{-0.8}$	24/28 = 0.86	23 $^{+2}_{-2}$	18 $^{+5}_{-5}$	1.7 $^{+0.5}_{-0.2}$
flare3	high	44 $^{+2}_{-2}$	0.004 $^{+1.203}_{-0.001}$	-0.03 $^{+0.03}_{-0.25}$	120/118 = 1.024	230 $^{+10}_{-10}$	140 $^{+10}_{-10}$	13 $^{+1}_{-1}$
	med	63 $^{+6}_{-6}$	7 $^{+2}_{-2}$	0.0 $^{+0.0}_{-0.1}$	75/61 = 1.24	130 $^{+10}_{-10}$	100 $^{+10}_{-4}$	9.7 $^{+1.0}_{-0.4}$
	low	62 $^{+6}_{-6}$	2.2 $^{+0.9}_{-0.9}$	-0.2 $^{+0.2}_{-0.3}$	148/132 = 1.122	31 $^{+4}_{-4}$	24 $^{+4}_{-3}$	2.3 $^{+0.3}_{-0.3}$
flare4	high	47 $^{+4}_{-4}$	0.8 $^{+0.9}_{-0.8}$	0.0 $^{+0.0}_{-0.3}$	72/69 = 1.049	110 $^{+10}_{-10}$	67 $^{+3}_{-3}$	6.3 $^{+0.3}_{-0.6}$
	med	57 $^{+5}_{-5}$	1 $^{+1}_{-1}$	-0.07 $^{+0.07}_{-0.39}$	93/80 = 1.171	65 $^{+6}_{-9}$	47 $^{+6}_{-6}$	4.4 $^{+0.4}_{-0.6}$
	low	64 $^{+7}_{-6}$	1 $^{+1}_{-1}$	0.0 $^{+0.0}_{-0.2}$	55/60 = 0.921	30 $^{+2}_{-3}$	24 $^{+2}_{-3}$	2.2 $^{+0.2}_{-0.2}$

NOTE—The table above lists spectral parameters from the flares. The first three flares correspond to OBSID 00012178006 and the last four flares correspond to OBSID 00012178037. Shown are the time (MJD - 58000), column densities, reflection fraction, C-stat/ ν values, absorbed and unabsorbed fluxes of the central engine, and Eddington fraction. The flares were fit with the same model used on the other spectra.

REFERENCES

- Arnaud, K. A. 1996, in *Astronomical Society of the Pacific Conference Series*, Vol. 101, *Astronomical Data Analysis Software and Systems V*, ed. G. H. Jacoby & J. Barnes, 17
- Balakrishnan, M., Tetarenko, B., Corrales, L., Reynolds, M., & Miller, J. M. 2019, *The Astronomer’s Telegram*, 12848, 1
- Belloni, T., Klein-Wolt, M., Méndez, M., van der Klis, M., & van Paradijs, J. 2000, *A&A*, 355, 271
- Blum, J. L., Miller, J. M., Fabian, A. C., et al. 2009, *ApJ*, 706, 60
- Boggs, P. T., & Rogers, J. E. 1990, *Statistical analysis of measurement error models and applications: proceedings of the AMS-IMS-SIAM joint summer research conference*, *Contemporary Mathematics Series*, vol 112, page 186
- Burrows, D. N., Hill, J. E., Nousek, J. A., et al. 2004, in *Society of Photo-Optical Instrumentation Engineers (SPIE) Conference Series*, Vol. 5165, *X-Ray and Gamma-Ray Instrumentation for Astronomy XIII*, ed. K. A. Flanagan & O. H. W. Siegmund, 201–216
- Cash, W. 1979, *ApJ*, 228, 939
- Corral-Santana, J. M., Casares, J., Muñoz-Darias, T., et al. 2016, *A&A*, 587, A61
- Emmanoulopoulos, D., Papadakis, I. E., Epitropakis, A., et al. 2016, *MNRAS*, 461, 1642
- Foster, A. R., Ji, L., Smith, R. K., & Brickhouse, N. S. 2012, *ApJ*, 756, 128
- Gehrels, N., Chincarini, G., Giommi, P., et al. 2004, *ApJ*, 611, 1005
- Hickox, R. C., Jones, C., Forman, W. R., et al. 2009, *ApJ*, 696, 891
- Homan, J., Neilsen, J., Steiner, J., et al. 2019, *The Astronomer’s Telegram*, 12742, 1
- Kammoun, E. S., Miller, J. M., Koss, M., et al. 2020, *ApJ*, 901, 161
- King, A. L., Miller, J. M., Raymond, J., Reynolds, M. T., & Morningstar, W. 2015, *ApJL*, 813, L37
- Li, S.-L., Xue, L., & Lu, J.-F. 2007, *ApJ*, 666, 368
- McClintock, J. E., & Remillard, R. A. 2006, *Black hole binaries*, Vol. 39, 157–213
- Merloni, A., & Nayakshin, S. 2006, *MNRAS*, 372, 728
- Miller, J. M., Balakrishnan, M., Reynolds, M., et al. 2019a, *The Astronomer’s Telegram*, 12771, 1
- Miller, J. M., Balakrishnan, M., Reynolds, M. T., et al. 2019b, *The Astronomer’s Telegram*, 12743, 1
- Miller, J. M., Raymond, J., Fabian, A., et al. 2006, *Nature*, 441, 953
- Miller, J. M., Parker, M. L., Fuerst, F., et al. 2013, *ApJL*, 775, L45
- Miller, J. M., Zoghbi, A., Raymond, J., et al. 2020, *arXiv e-prints*, arXiv:2007.07005
- Mirabel, I. F., & Rodríguez, L. F. 1994, *Nature*, 371, 46
- . 1999, *ARA&A*, 37, 409
- Miyamoto, S., Iga, S., Kitamoto, S., & Kamado, Y. 1993, *ApJL*, 403, L39
- Miyamoto, S., & Kitamoto, S. 1991, *ApJ*, 374, 741
- Morningstar, W. R., Miller, J. M., Reynolds, M. T., & Maitra, D. 2014, *ApJL*, 786, L20
- Motta, S., Williams, D., Fender, R., et al. 2019, *The Astronomer’s Telegram*, 12773, 1
- Motta, S. E., Kajava, J. J. E., Sánchez-Fernández, C., Giustini, M., & Kuulkers, E. 2017, *MNRAS*, 468, 981
- Negoro, H., Tachibana, Y., Kawai, N., et al. 2018, *The Astronomer’s Telegram*, 11828, 1
- Neilsen, J., Homan, J., Steiner, J. F., et al. 2020, *ApJ*, 902, 152
- Neilsen, J., Remillard, R. A., & Lee, J. C. 2012, *ApJ*, 750, 71
- Ponti, G., Fender, R. P., Begelman, M. C., et al. 2012, *MNRAS*, 422, L11
- Reid, M. J., McClintock, J. E., Steiner, J. F., et al. 2014, *ApJ*, 796, 2
- Remillard, R. A., & McClintock, J. E. 2006, *ARA&A*, 44, 49
- Reynolds, M., & Miller, J. M. 2013, in *AAS/High Energy Astrophysics Division*, Vol. 13, *AAS/High Energy Astrophysics Division #13*, 126.23
- Rykoff, E. S., Miller, J. M., Steeghs, D., & Torres, M. A. P. 2007, *ApJ*, 666, 1129
- Takagi, R., Kobayashi, K., Negoro, H., et al. 2020, *The Astronomer’s Telegram*, 13478, 1
- Tetarenko, B. E., Sivakoff, G. R., Heinke, C. O., & Gladstone, J. C. 2016, *ApJS*, 222, 15
- Trushkin, S. A., Nizhelskij, N. A., Tsybulev, P. G., Bursov, N. N., & Shevchenko, A. V. 2019a, *The Astronomer’s Telegram*, 12855, 1
- . 2019b, *The Astronomer’s Telegram*, 13304, 1
- Zoghbi, A., Miller, J. M., King, A. L., et al. 2016, *ApJ*, 833, 165